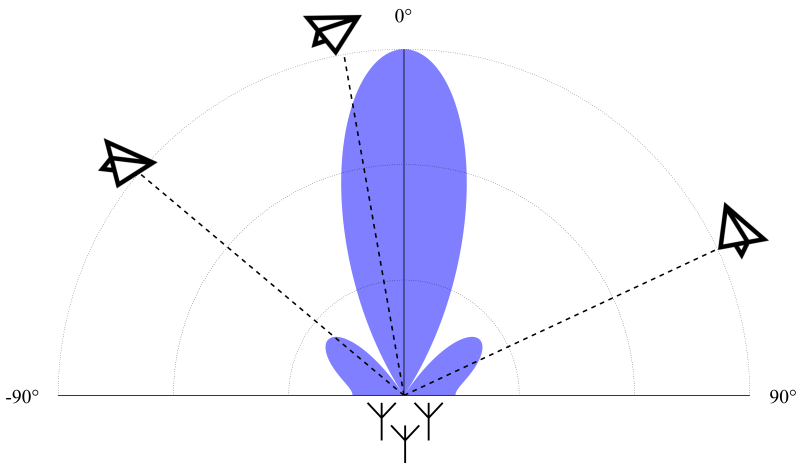

Direction of Arrival Estimations for a Secondary Surveillance Radar

Comparing the performance of DOA estimation algorithms for two different SSR hardware architectures

Master's thesis in Wireless Photonics and Space Engineering

FILIP BERGQVIST

DEPARTMENT OF ELECTRICAL ENGINEERING

CHALMERS UNIVERSITY OF TECHNOLOGY
Gothenburg, Sweden 2025
www.chalmers.se

Master's thesis 2025

Direction of Arrival Estimations for a Secondary Surveillance Radar

Comparing the performance of DOA estimation algorithms for two different SSR hardware architectures

Filip Bergqvist

CHALMERS
UNIVERSITY OF TECHNOLOGY

Department of Electrical Engineering
Division of Signal Processing and Biomedical Engineering, Electrical Engineering
Chalmers University of Technology
Gothenburg, Sweden 2025

Direction of Arrival Estimations for a Secondary Surveillance Radar
Comparing the performance of DOA estimation algorithms for two different SSR hardware architectures
Filip Bergqvist

Supervisor: Ida-Maria Svensson & Mattias Wiklund, SAAB Surveillance
Examiner: Tomas McKelvey, Department of Electrical Engineering

Master's Thesis 2025
Department of Electrical Engineering
Division of Signal Processing and Biomedical Engineering, Electrical Engineering
Chalmers University of Technology
SE-412 96 Gothenburg
Telephone +46 31 772 1000

Cover: Antenna directional gain in an airspace with three aircraft. The aircraft's positions are indicated by dashed lines.

Typeset in LaTeX
Printed by Chalmers Reproservice
Gothenburg, Sweden 2025

Direction of Arrival Estimations for a Secondary Surveillance Radar
Comparing the performance of DOA estimation algorithms for two different SSR hardware architectures
Filip Bergqvist
Department of Electrical Engineering
Chalmers University of Technology

Abstract

In aviation, Secondary Surveillance Radar (SSR) systems are used to generate situational images of an airspace. Through standardized communication protocols, aircraft reply to interrogations from SSR stations with their identity. By time-of-flight calculations and Direction of Arrival (DOA) estimations performed on the reply, the aircraft's position can be determined. Since the frequencies used for the SSR communications are heavily trafficked, SSR experiences many problems related to interfering signals. This thesis investigates the DOA estimation performance of an airborne SSR system, where a digital hardware architecture is compared to an analog hardware architecture, exploring their potential in relation to the occurrence of interfering signals. The analog architecture, used as a benchmark, employs a phase monopulse algorithm for DOA estimation, while a few different algorithms are analyzed for the digital architecture. Through Monte-Carlo style simulations of Mode S replies, incorporating noise and randomized interfering signals, the performance of each architecture and algorithm is studied. ESPRIT is concluded to be the most prominent algorithm used with the digital architecture. Although not delivering as precise DOA estimations as the analog architecture, the digital architecture outperforms the analog in terms of simultaneous coverage and probability to decode the signals. The results suggest that, by leveraging the digital architecture's broader field of view by making additional estimates, further improvements of the digital architecture's estimate precision are possible. Future research could for example focus on methods to enhance digital DOA accuracy under practical operational constraints.

Keywords: Secondary Surveillance Radar, Mode S, Direction of Arrival, Signal processing, Interfering signals, Monopulse, ESPRIT, MUSIC, Higher-Order Yule-Walker.

Acknowledgements

I would like to express my sincere gratitude to my supervisors at SAAB, Ida-Maria Svensson and Mattias Wiklund. Thank you for all the discussions, support, and input throughout this project. It has been both educational and intriguing to study and write about this subject under your guidance. I also wish to thank the IFF team at SAAB for making the process of writing this thesis enjoyable, with special thanks to Erik Rilby for his help during my onboarding and first day.

I would also like to thank Tomas McKelvey for acting as the examiner from Chalmers, making the thesis possible.

Finally, I wish to thank everyone who has made the past five years at Chalmers educational, memorable and enriching.

Filip Bergqvist, Gothenburg, June 2025

List of Acronyms

Below is the list of acronyms that have been used throughout this thesis listed in alphabetical order:

DOA	Direction Of Arrival
IFF	Identification Friend or Foe
SSR	Secondary Surveillance Radar
ATC	Air Traffic Control
PPM	Pulse Position Modulation
MUSIC	MUltiple SIgnal Classification
ESPRIT	Estimation of Signal Parameters by Rotational Invariance Technique
HOYW	Higher-Order Yule-Walker
LOS	Line Of Sight
ICAO	International Civil Aviation Organization
LCMP	Linear Constraint Minimum Power

Nomenclature

Below is the nomenclature of indices, sets, parameters, and variables that have been used throughout this thesis.

Parameters & variables

N	Antenna elements in an array
K	Time samples in a measurement
M	Number of signals in a measurement
θ	Angle in the azimuth plane
φ	Array phase
R_x	Covariance matrix of variable x
U_s	Signal subspace
U_n	Noise subspace
f	Frequency
$a(\theta)$	Steering vector
A	Steering matrix
c	Speed of light
λ	Wavelength, Interfering intensity, Eigenvalue

List of Figures

2.1 A FRUIT scenario where two transponders reply to one interrogator each, but the isotropic replies reach both interrogators. 6
2.2 Structure of a Mode S reply [6, fig.3-6 p.90]. The first 8 µs is a preamble followed by a PPM data segment where a 1-bit is described by a peak followed by a null in the electric field, and a 0 bit is described by a null followed by a peak. 7
2.3 Example of directive gain of an antenna. A main lobe pointing in 0°. The point on one side where the gain is $-3\,\mathrm{dB}$ from the peak is marked and a sector is drawn displaying the 3 dB lobe width, $\theta_{3\,\mathrm{dB}}$. Note that the figure is not to scale . 8
2.4 Geometry of waves transmitted from a ULA in a direction θ. The difference in propagation distance between two adjacent elements in a direction θ is shown as $d_a \sin\theta$. Note here that the scales are arbitrary and that the distance to the plane wavefronts needs to be very large ($\gg \lambda$). 9
2.5 Analog architecture of an antenna array with six elements. Each element is connected to a phase shifter. The three leftmost and rightmost elements are summed up separately and added or subtracted to form sum and delta channels respectively. These channels are digitized. 11
2.6 Digital architecture of an antenna array with six elements. Each element is connected to an ADC and the phase shifts are introduced to the signal in software. 11
2.7 Signal arriving to a ULA with a Direction Of Arrival (DOA) θ. The additional distance a wave needs to propagate to reach the next element is seen to be $d_a \sin\theta$. 12
2.8 An example of directional gain of the sum and delta lobes. Lobes are steered in $\theta_0 = 30°$. The sum lobe is centered in θ_0 and the delta lobe has a null in θ_0. . . . 16
2.9 A description of the analog signal processing chain. A reply is detected and decoded before the good samples of an SOI, which are not as disturbed by interfering signals, are used in a DOA estimate algorithm. The result is a decoded signal and a DOA. 21
2.10 Proposed signal processing chain for a digital SSR architecture. The continuous stream of samples is first split up in segments that are processed. In each segment the number of signals is estimated and a preliminary DOA estimation is made. For each signal in the segment, adaptive beamforming is performed to suppress all other signals. The remaining signal is then decoded. One at a time, all of these decoded signals are individually considered as SOIs with all the samples they consist of. Another DOA estimation is made on these samples for each SOI. The DOA that was present in all segments of this SOI is assumed to belong to the SOI and is paired with the decoded SOI. 22

3.1 Example with three interfering signals placed with different amplitudes and starting times. Shown during a long reply time window. 26
3.2 The simulation space for simulating the algorithms (Not to scale). A red line at 80° marks the end of the simulation space for SOIs. Circle sectors with notches are where SOIs were placed for DOA estimations. A red area within 100 km marks where no signals were allowed. A blue line shows the antenna element directional gain approximate appearance. 29
3.3 Block diagram of how the analog DOA estimation was simulated. For a time window matched to the SOI, the samples with pulses were selected. The DOA was estimated for all lobe steering directions and the best estimate was chosen. It was then determined if the signal could have been decoded. The hexagon is the possible output of the simulation. 30
3.4 Block diagram of how digital DOA estimations was simulated. For a time window matched to the SOI, the samples without SOI pulses were set to zero. DOA estimates were done and the best estimate was selected as an estimate for the SOI DOA. Adaptive beamforming was used to suppress the interfering signals and amplify the SOI before determining if the SOI would have been possible to decode. The hexagon indicates the possible output of the simulation. 31

4.1 Algorithm's performance for an intensity of 0.0 interfering signals/km^{2}s. The error statistics for each algorithm are presented above P_{dec}. P_{dec} is constantly 100% for all algorithms since no SIR quota can be made. There are slight bumps in the monopulse bias and standard deviation because of the discrete array steering directions. The standard deviation increases with larger DOAs because of increased sensitivity at higher DOAs as explained in Appendix A.1. The mean bias error of all algorithms deviates at 75°, which caused by smaller antenna size orthogonal to higher DOAs. 34
4.2 Algorithm's performance for an intensity of 0.0026 interfering signals/km^{2}s. The error statistics for each algorithm are presented above P_{dec}. Note that plot (c) and (d) have different scales on the vertical axis. The presence of interfering signals enables calculations of SIR quotas, yielding scenarios where SOI cannot be decoded, which is represented by P_{dec} plots. HOYW's poor P_{dec} and low precision describe the algorithm's poor performance at the presence of single interfering signals. MUSIC also displays low precision, but its higher P_{dec} indicates better handling of interfering signals compared to HOYW. MUSIC's lower P_{dec} for higher SNR might be caused by the usage of the noise subspace in the algorithm. The high P_{dec} for ESPRIT implies that the algorithm is good at estimating DOAs of all signals, resulting in appropriate beamforming suppressing interfering signals. 36
4.3 Algorithm's performance for an intensity of 0.0066 interfering signals/km^{2}s. The error statistics for each algorithm are presented above P_{dec}. Note that plot (c) has a different scale on the vertical axis. HOYW is not included because of the very poor P_{dec}. ESPRIT displays a greater SNR dependency for DOAs around 60°. P_{dec} is affected for all algorithms compared to the results in Figure 4.2. Monopulse displays a hill in standard deviation centered around 30°, probably caused by discrete array steering directions. 38

4.4 Algorithm's performance for an intensity of 0.013 interfering signals/km^{2}s. The error statistics for each algorithm are presented above P_{dec}. Note that the plot (c) has a different scale on the vertical axis. Results for MUSIC show nearly no change from Figure 4.3. Simulations with more than five signals are more common at this interfering intensity. Since ESPRIT and MUSIC are capable of estimating at most five signals, this impacts their P_{dec}. 40
4.5 Algorithm's performance when one interfering signal has a fixed DOA at 36°. This is marked with a vertical black line in the plot. The error statistics for each algorithm are presented above P_{dec}. Monopulse shows effects of discrete array steering directions with sections of higher or lower standard deviation and P_{dec}. In array steering direction covering DOAs $[-35°, 0°]$, the interfering signal at 36° lies in a null of directive gain from conventional beamforming. ESPRIT's capability to account for interfering signals is seen by the way its precision is mainly affected around the interfering signal, but generally unaffected for DOAs far away from it. 42
4.6 Directional gain of sum and delta channels for an antenna array steered in $\theta_0 = -30°$ by conventional beamforming. An interfering signal marked at 36° inside a gain null. 43
4.7 Algorithm's performance when two interfering signals have fixed DOAs at −10° and 45°. These are marked with vertical black lines in the plot. The error statistics for each algorithm are presented above P_{dec}. ESPRIT still manages to account for the interfering signals, yielding results that are not as affected by them far away from the interfering signals. The monopulse has problems where the interfering signals appear in most main or side lobes, disturbing the estimates. For monopulse estimates above 40° the lobe is very disturbed, causing lower SNR environment simulations to yield extremely poor P_{dec}. 44
4.8 Algorithm's performance when two interfering signals have fixed DOAs at 40° and 47°. These are marked with vertical black lines in the plot. The error statistics for each algorithm are presented above P_{dec}. ESPRIT is capable of compensating for both interfering signals, so that estimates far away from them are seemingly unaffected. The monopulse still experiences difficulties with interfering signals in side lobes. Lobes covering DOAs greater than 40° are still very disturbed. 45
4.9 Directional gain of sum and delta channels for an antenna array steered in $\theta_0 = -45°$. Interfering signals are marked at 40° and 47° inside a sum side lobe. An interfering signal marked at 47° also inside delta side lobe. 46

A.1 Theoretical maximum error when optimal DOA estimation is made assuming signal frequency $f = 1090\,\text{MHz}$. Note that the y-axis is in logarithmic scale. . . I

List of Tables

3.1 Interfering occurrence intensities per area and time. 26

5.1 Table describing differences in estimate precision and accuracy, P_{dec}, simultaneous coverage, interference robustness and SNR robustness of the digital SSR architecture in relation to the analog architecture. Note that the classification of the performance is somewhat arbitrary and only done for scenarios where the architectures could decode the signal. 51

Contents

List of Acronyms **v**

Nomenclature **vii**

List of Figures **ix**

List of Tables **xiii**

1 Introduction **1**

2 Theory **5**
2.1 Secondary Surveillance Radar . . . 5
2.2 Mode S . . . 6
2.3 Antennas and hardware . . . 7
2.3.1 Uniform Linear Arrays . . . 8
2.3.2 SSR hardware architecture . . . 10
2.4 Signal model . . . 12
2.4.1 Covariance matrix model and subspaces . . . 13
2.4.2 Signal environment . . . 14
2.5 Direction of arrival estimation algorithms . . . 15
2.5.1 Monopulse algorithm . . . 15
2.5.2 ESPRIT . . . 17
2.5.3 MUSIC . . . 18
2.5.4 Higher Order Yule-Walker algorithm . . . 19
2.6 Signal processing chain . . . 20
2.7 Statistics . . . 23

3 Methods **25**
3.1 Antenna model . . . 25
3.2 Environment . . . 25
3.3 Signals . . . 27
3.4 Simulation . . . 27
3.4.1 General simulations . . . 29
3.4.2 Fixed interfering signals . . . 31

4 Results and analysis **33**
4.1 General simulations . . . 33

4.2 Fixed interfering signals 41

5 Discussion **49**
5.1 Comparison of SSR architectures 49
5.2 Impacts of assumptions 51
5.3 Continued work 52

6 Conclusion **55**

A Appendix **I**
A.1 Theoretical error limit I
A.2 Line of sight range II
A.3 Uniform distribution of points on a disk II

1
Introduction

Since the first radio was invented by Guglielmo Marconi in 1896 [1], electromagnetic (EM) wave theory has been a key component of modern wireless communications. With the realization that EM pulses intended for communications could reflect off some surfaces, a Radio Detection And Ranging (RADAR) device was invented in 1904 [2]. While the technology was initially intended to find ships in dense fog, the attention was soon shifted to the skies, as the airspace became an important battleground in the Second World War. In wartime however, determining the position of an aircraft is not enough. The need to identify an aircraft as friendly or hostile meant that the primary radar needed a complement. The solution to this is the Identification, Friend or Foe (IFF) system, where a secondary surveillance radar (SSR) sends an interrogation to an aircraft, which reply with an identification. By performing range calculations and direction of arrival (DOA) estimation on the reply, it is possible to determine the position of the aircraft.

Today, as the civilian aviation sector has grown and caused densely trafficked airspaces, the use of SSRs is highly relevant. The civilian application focuses on creating situational images of an airspace to help automated systems and air traffic control (ATC) units safely guide aircraft through airspaces. To create this situational image, a traditional, primary surveillance radar (PSR) is used together with an SSR. The combination of these two systems allows for detection and identification of the aircraft present in the airspace.

Today SSR systems face some problems. Since the airspaces are heavily trafficked, the frequencies used by SSR systems are very busy. This increases the risk of signals interfering with each other, making them harder to decode and degrading the performance of the signal processing algorithms used to determine the position of the aircraft. As radar technology has evolved, its applications have expanded far beyond traditional uses, now applied in diverse fields such as automotive safety systems and forest ecosystem monitoring [3]. This has contributed to a development of the hardware used for radars, making it cheaper and less power consuming [4]. Modern radars commonly utilize array antennas consisting of several antenna elements, as well as different hardware architecture for handling the channels through which the software interacts with the antenna elements.

To increase the performance of position measurements for an SSR system, DOA estimations algorithms can leverage the properties of antenna arrays. Because the elements of an antenna array are spread out, the distance from each element to a target is slightly different. This distance variation results in the signal reaching each antenna element at different times, thereby creating phase shifts between the signals received by the different elements. With signal processing techniques, these phase differences can be used to estimate the DOA. Depending on

how the elements are combined to channel the signal to the software, different algorithms may be utilized. While a traditional analog radar architecture allows for some algorithms to be applied, a digital radar architecture, where all antenna elements have their own channel, enables a larger number of algorithms.

Because digital radar architectures are not as common for SSR systems, the potential in terms of SSR system performance is relatively unknown. An SSR system has two main tasks: detecting the presence of a signal, so that it can be decoded, and measure on the signal to determine the position of the target. Methods to detect signals and decode them can be improved by digital beamforming, which was studied in the context of an SSR in a previous master's thesis [5]. In this thesis, focus instead lies on the DOA estimates which are made on the replies. The aim is to compare DOA estimation for a common analog SSR hardware architecture with different DOA estimation algorithms for a suggested implementation of a digital SSR architecture.

Through Monte-Carlo style simulations, the analog architecture with a monopulse algorithm is compared to some different algorithms implemented in a digital architecture. The simulations are performed for sets of environments with noise and randomized interfering signals. By studying the errors in terms of standard deviation and mean bias error together with the probability of decoding, the performance of algorithms are compared and characterized. The monopulse algorithm and most promising digital algorithm are also studied further in more specific environments to further characterize their behaviors and strengths. A conclusion regarding strengths and weaknesses is made from these results.

2
Theory

In this chapter, the theory used in this thesis is presented.

2.1 Secondary Surveillance Radar

In aviation, safety is a main concern since the consequences of an accident could be huge with many casualties. To avoid any accidents, such as collisions, air traffic control (ATC) units in densely trafficked airspace communicate with aircraft to safely guide them in the airspace.

One tool that is used for this task is a secondary surveillance radar (SSR). An SSR is a system that relies on communication between an interrogator (typically some sort of ATC post) and a transponder (typically an aircraft). The interrogator sends an interrogation and when the transponder receives an interrogation it sends a reply. For all parts to understand each other, the interrogations and replies follow different protocols, called modes, that determine what information to include and how it should be structured.

The replies typically consist of information about the aircraft, such as identity and altitude, depending on the mode. However, to determine the position of an aircraft, measurements on the reply signal are generally required. To find the distance from the interrogator to the transponder, the modes dictate the time a transponder needs to wait after receiving an interrogation before they transmit a reply. This allows for a time of flight measurement to be made on the reply. To determine the azimuth angle (in a horizontal plane) of the transponder relative to the interrogator, direction of arrival (DOA) estimation algorithms are used.

SSR systems experience some challenges. Most notably, the used frequencies are heavily trafficked since all aviation SSR communications are performed on the L frequency band where the interrogations are sent on 1030 MHz and replies on 1090 MHz. By utilizing beamforming, explained in Section 2.3.1, the interrogations are sent in specific directions, but the replies are transmitted isotropically, in all directions. This means that a transponder responding to the interrogation from a specific interrogator, sends its response to all interrogators that are within range.

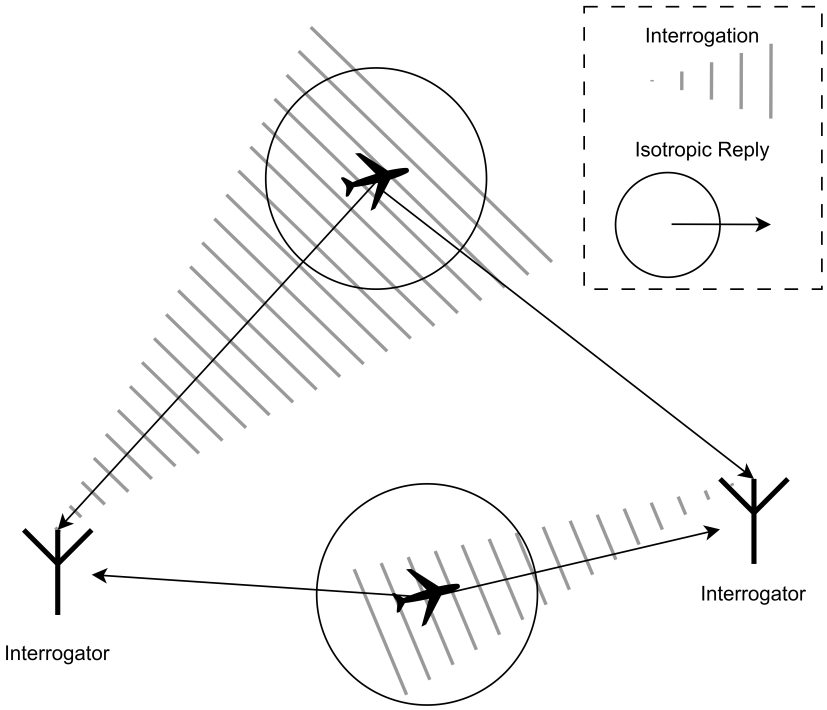

Figure 2.1: A FRUIT scenario where two transponders reply to one interrogator each, but the isotropic replies reach both interrogators.

An example of this is shown in Figure 2.1. This is often referred to as false replies unsynchronized in time (FRUIT). If the signals are sent on the same or a similar mode, the FRUIT arriving at an interrogator is indistinguishable from replies that the interrogator requested. Therefore, these interfere with the signal of interest (SOI), possibly making it impossible to decode.

2.2 Mode S

For the interrogators and transponders to be able to communicate with each other, their communication needs to follow certain protocols, called modes. The most common, and in most geographical regions required mode to use is Mode S. The Mode S replies are Pulse Position Modulated (PPM), where the position of a 1-bit in time implies certain information. In the transmitted fields, the 0-bit is described by a null followed by a pulse. The 1-bit is described by pulse followed by a null of the transmitted field. This means that in the transmitted data, half of the time samples consist of pulses and half of the time samples consist of nulls.

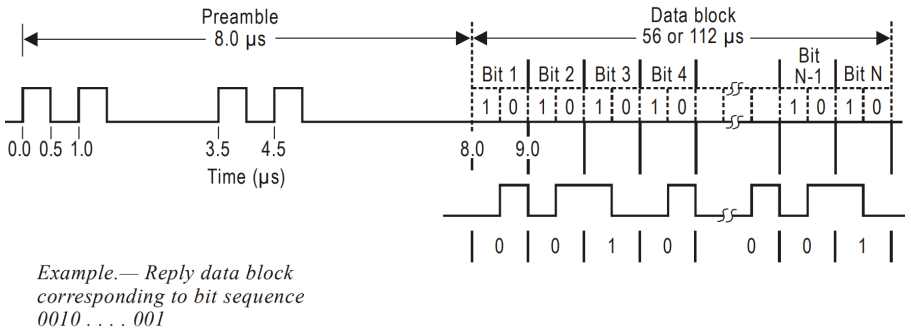

Figure 2.2: Structure of a Mode S reply [6, fig.3-6 p.90]. The first 8 µs is a preamble followed by a PPM data segment where a 1-bit is described by a peak followed by a null in the electric field, and a 0 bit is described by a null followed by a peak.

To identify a Mode S reply, each reply is proceeded by a preamble of 4 pulses spread out during 8 µs, followed by a data block. A Mode S transponder may transmit a short data block consisting of 56 bits during 56 µs or a longer data block with 112 bits during 112 µs. For both lengths the data rate becomes 1 bit/µs. An example of a Mode S reply can be seen in Figure 2.2.

The usage of Mode S is regulated by the International Civil Aviation Organization (ICAO). Some relevant restrains they imply are that a transponders are required to have the capability to transmit a minimum of 50 replies per second, and that the carrier frequency of a reply may at most differ 1 MHz from 1090 MHz [6, Ch.3, p.12]. Other regulations include, among other topics, how often a transponder is allowed to send a reply and in what cases a transponder is required to reply to an interrogation.

2.3 Antennas and hardware

Antennas are a key component in a Secondary Surveillance Radar (SSR) system, where they are used as instruments to transmit or receive electromagnetic waves by converting them from or to electric signals, respectively. By designing the physical geometry and other properties of an antenna, different characteristics can be achieved. By combining two or more antenna elements, larger structures can be made, resulting in different combined characteristics.

One way to characterize an antenna is by its directive gain [7, Ch. 2]. This expresses how much power an antenna radiates in a certain direction, $P(\vec{r})$, in relation to how much it would radiate in any direction, $P_{\text{isotropic}}$, if it were isotropically radiating. For simplicity, this value is often described in "decibel relative to the isotropic case" dBi as

$$G(\vec{r})|_{\text{dBi}} = 10 \log \left| \frac{P(\vec{r})}{P_{\text{isotropic}}} \right| \tag{2.1}$$

where $\vec{r}$ is a unit vector. This property can be described for both individual elements and larger antenna structures. Generally, the direction $\vec{r}$ is replaced by an angle in a plane where the directive gain is studied. In this thesis, the angle θ is used as an angle relative to the antenna normal in the azimuth (horizontal) plane as in Figure 2.3.

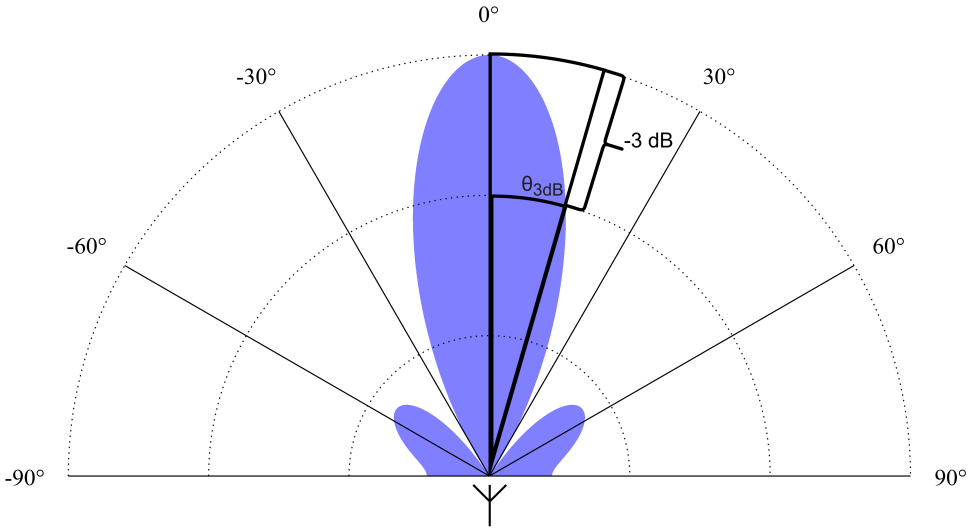

Figure 2.3: Example of directive gain of an antenna. A main lobe pointing in 0°. The point on one side where the gain is −3 dB from the peak is marked and a sector is drawn displaying the 3 dB lobe width, $\theta_{3\,\mathrm{dB}}$. Note that the figure is not to scale

When there is high directive gain in a sector around an angle θ_0, this is called an antenna lobe. A lobe is often described with its "3 dB-width", which is how large an angle from the peak directive gain of the lobe to a point where the directive gain is half of the peak in the lobe. Similarly, a "full 3 dB-width" is the angle from one of the 3 dB points to the other. The lobe sizes of an antenna are generally a consequence of the design of the antenna. The 3 dB-width in a direction mainly depends on the wavelength λ and antenna size L in the lobe plane as

$$\theta_{3\,\mathrm{dB}} \propto \frac{\lambda}{L}. \tag{2.2}$$

From this expression, it becomes clear that a larger antenna allows for a more narrow main lobe. With a narrow main lobe, it is possible to measure with a higher resolution.

2.3.1 Uniform Linear Arrays

A common practice when creating larger antenna structures, that is used in this thesis, is to place N antenna elements in a straight line. With a uniform linear spacing of d_a between the elements, this is called a Uniform Linear Array (ULA) [8, Ch. 2.3]. With a transmitting ULA, a plane electromagnetic wave from the different elements in a certain direction θ experience a difference in propagated distance. Given that the bandwidth of the signals are narrow enough, this distance is small enough to be irrelevant for the amplitude, but still relevant for the phase of the waves. As the phase differences alter with the direction, the waves interfere positively or negatively, meaning that the directional gain changes with the azimuth angle θ. Utilizing this, different techniques can be applied to steer the lobes of the array.

Steering can be achieved in different ways. In this thesis, two beamforming methods are utilized. One of these is the so-called conventional beamforming. It is done by introducing a constant phase shift in the feed of each element. For the fields from the different elements to interfere positively in a direction θ_0 from the antenna normal, the phases of their fields need to coincide in that direction.

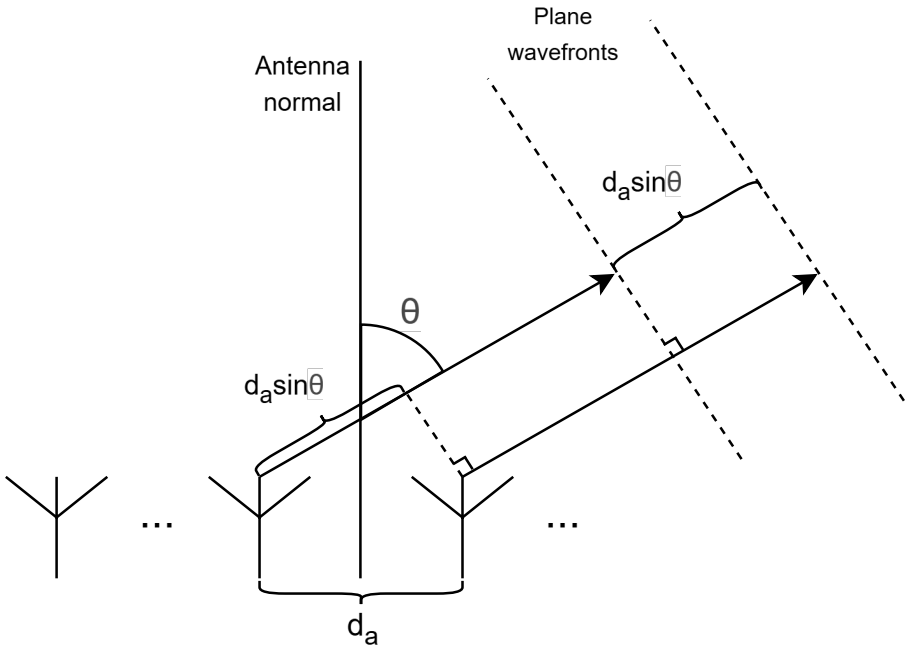

Figure 2.4: Geometry of waves transmitted from a ULA in a direction θ. The difference in propagation distance between two adjacent elements in a direction θ is shown as $d_a \sin\theta$. Note here that the scales are arbitrary and that the distance to the plane wavefronts needs to be very large ($\gg \lambda$).

From geometry seen in Figure 2.4, one can deduct that generating a phase difference between each element as

$$\Delta\varphi(\theta_0) = \frac{2\pi d_a \sin\theta_0}{\lambda} \tag{2.3}$$

means that the main lobe is steered in the direction θ_0. The vector describing the weighting of the signal being fed to the elements is then

$$w(\theta_0) = \begin{bmatrix} 1 & e^{i\Delta\varphi(\theta_0)} & \dots & e^{i(N-1)\Delta\varphi(\theta_0)} \end{bmatrix}^T \tag{2.4}$$

where N is the number of antenna elements in the array. An array typically has a main lobe that can be steered in this way.

There are directions where positive interference of some individual elements occurs unintentionally. These directions are referred to as side lobes. If the fields of all elements interfere positively outside of the main lobe, this is called a grating lobe. Because the gain in grating lobes are equal to the gain in the main lobe, these might cause problems such as ambiguities in position measurements. To avoid grating lobes, the distance between the antenna elements needs to be $d_a \leq \frac{\lambda}{2}$.

The second beamforming method used in this thesis is the Linear Constraint Minimum Power, which is an adaptive algorithm and requires a digital SSR architecture, discussed in Section 2.3.2. This algorithm is derived and studied more thoroughly for the context of an SSR in [5]. The result of this derivation however, is that the different elements are fed with weighted

versions of the signal. The weights come from a weighting vector

$$w^H = g^H (A^H R_y^{-1} A)^{-1} A^H R_y^{-1}, \tag{2.5}$$

where the vector g decides what directions in the Vandermonde steering matrix A, to amplify or suppress and R_y is the covariance matrix from the measurement. These variables are explained further in Section 2.4. By formulating an optimization problem and imposing certain constraints as the weighting vector g in (2.5), the directive gain can be amplified in certain directions and suppressed in others.

To calculate the directional gain in a direction θ, this weighting vector w calculated from a beamforming technique can be multiplied with a weighting vector in that direction θ, as

$$G_(\theta) = w^H \cdot a(\theta) \tag{2.6}$$

where $a(\theta)$ is the weighting vector from a conventional beamforming in the direction θ.

2.3.2 SSR hardware architecture

The physical design of an antenna array might impact the directional gain of the antenna. But the architecture for handling the signals fed to or received by the elements impacts the possibilities for what can be done with the signals. For a receiving system, the aim is to digitize signals using Analog to Digital Converters (ADC) so that the signals can be processed and information can be extracted. To transmit, the signals are instead sent the other way. Hence the architectures can generally be used to both transmit and receive. Therefore, the receiving case is explained below, but the transmitting case follows by analyzing the processing chain in the reversed order.

To steer antenna lobes conventionally, there are generally two approaches to introduce phase shifts to the individual elements. One is to do it in hardware, by placing phase shifters by the antenna elements. Another is to introduce the phase shifts to each channel digitally in software. Traditionally, hardware for digital SSR structures has been more expensive, power consuming and impractical [4], which has made the analog architecture more common today.

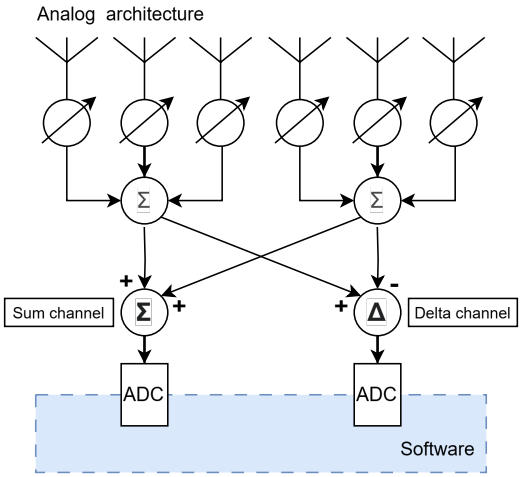

Figure 2.5: Analog architecture of an antenna array with six elements. Each element is connected to a phase shifter. The three leftmost and rightmost elements are summed up separately and added or subtracted to form sum and delta channels respectively. These channels are digitized.

The architecture illustrated in Figure 2.5 is a typical analog architecture, which conventionally steers lobes by introducing phase shifts in the channels from each antenna element before summarizing the left and right half of the channels. One half is then added to the other to create a sum channel, and subtracted to create a delta channel. These two channels are then connected to an ADC that digitizes the signals for the software to process.

In the digital system, because the element weighting is done in software, each channel needs to be kept separate from the others so that the phases are not mixed. This means that there needs to be one channel per antenna element all the way from the antenna to the software interface. While one ADC is needed for each element, a lot of other hardware can be removed. This allows for a simpler hardware architecture with the software closer to the antenna elements.

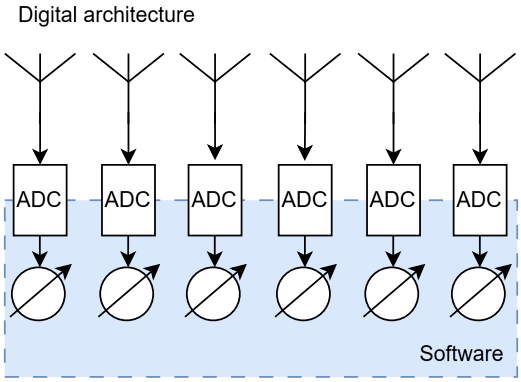

Figure 2.6: Digital architecture of an antenna array with six elements. Each element is connected to an ADC and the phase shifts are introduced to the signal in software.

In software, it is possible to introduce element weighting to also enable adaptive beamforming. Since the data from the elements are separate from each other and unmodified, it is also possible

to apply beamforming several times in different directions for the same received data. With the data from the individual elements, a number of opportunities are enabled. This architecture is also cheaper to mass produce since software can be copied without any additional costs as opposed to hardware. This is why the digital architecture is increasingly common for modern radars and antenna systems. Some of these signal processing possibilities that are enabled are explored in this thesis.

2.4 Signal model

An electromagnetic wave propagating in a direction through space does so with the speed of light and a certain frequency f. By altering the signal in time, some information can be placed on the wave, creating a signal. When the wave propagates, its phase changes in space as $e^{i2\pi tc/\lambda} = e^{i2\pi r/\lambda}$ where $ct = r$ is the length a signal propagates. When a signal is transmitted isotropically, its carrying wave is initially spherically shaped around the source antenna. But as the wave propagates, the large spherical wave can be approximated as a plane wave in the same way that the Earth may appear flat while in fact being a sphere. This is commonly described as the far field approximation for circular waves [9]. It is especially useful for describing the direction a wave is traveling in, since a plane wave can have one unique direction, while a circular wave does not. This way of describing the direction of a wave becomes crucial when deriving direction finding techniques.

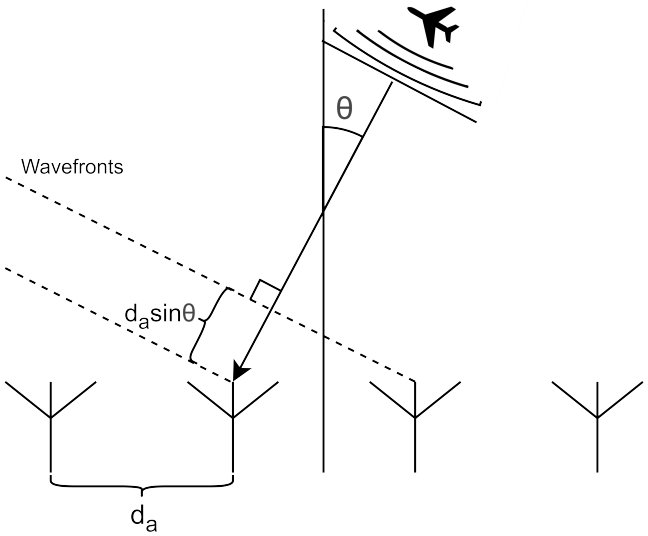

Figure 2.7: Signal arriving to a ULA with a Direction Of Arrival (DOA) θ. The additional distance a wave needs to propagate to reach the next element is seen to be $d_a \sin\theta$.

To determine the DOA of a signal, some assumptions need to be made about the signal and array that receives it. For this, the geometry in Figure 2.7 is used. When a signal arrives at a ULA, the individual antenna elements receive the signal with small time delays depending on the DOA of the signal. Between two elements, the signal needs to propagate an additional distance

$$\ell = d_a \sin\theta \tag{2.7}$$

to arrive at the neighboring element. This results in a time delay as $\Delta t = \ell/c$ which is negligible due to the high speed of light. In phase however, this distance becomes relevant. Since the signal propagates as $e^{2i\pi ft}$ in time, the phase shift of the signal that adjacent antenna elements experience is

$$\Delta\varphi = 2\pi f \Delta t = 2\pi \frac{c}{\lambda}\frac{d_a \sin\theta}{c} = \frac{2\pi d_a \sin\theta}{\lambda}. \tag{2.8}$$

This is referred to as the array phase in this thesis. This is in essence the same as (2.3) for conventional beamforming, which is derived from the same signal model. With this equation, one can describe an ideal case of a time varying signal $x(t)$ that arrives onto a noise free array as the sampled signal $x(t_k)$ multiplied with a Vandermonde steering vector $\vec{a}(\theta)$ containing these phase differences. This becomes

$$\begin{aligned} y(t) = &\vec{a}(\theta)x(t) = \begin{bmatrix} 1 \\ e^{i\Delta\varphi} \\ \vdots \\ e^{ni\Delta\varphi} \\ \vdots \\ e^{(N-1)i\Delta\varphi} \end{bmatrix} \begin{bmatrix} x(t_1) & \dots & x(t_K) \end{bmatrix} = \\ &\begin{bmatrix} x(t_1) & \dots & x(t_K) \\ \vdots & x(t_k)e^{ni\Delta\varphi} & \vdots \\ x(t_1)e^{(N-1)i\Delta\varphi} & \dots & x(t_K)e^{(N-1)i\Delta\varphi} \end{bmatrix}. \end{aligned} \tag{2.9}$$

Here there are K time samples, called snapshots, and N antenna elements. By then expanding the model to allow for M signals, the Vandermonde matrix $A = \begin{bmatrix} \vec{a}(\theta_1) & \dots & \vec{a}(\theta_M) \end{bmatrix} \in \mathbb{C}^{N\times M}$ is introduced together with the new signal matrix $\vec{x}(t) = \begin{bmatrix} x_1(t) & \dots & x_M(t) \end{bmatrix}^T \in \mathbb{C}^{M\times K}$. Noise is also introduced as $\vec{e}(t) = \begin{bmatrix} e_0(t) & \dots & e_{N-1}(t) \end{bmatrix}^T \in \mathbb{C}^{N\times K}$ so that the expanded signal model becomes

$$\begin{aligned} &y(t) = A\vec{x}(t) + \vec{e}(t) = \\ &\begin{bmatrix} 1 & \dots & 1 \\ e^{i\Delta\varphi_1} & \dots & e^{i\Delta\varphi_M} \\ \vdots & e^{ni\Delta\varphi_m} & \vdots \\ e^{(N-1)i\Delta\varphi_1} & \dots & e^{(N-1)i\Delta\varphi_M} \end{bmatrix} \begin{bmatrix} x_1(t_1) & \dots & x_1(t_K) \\ \vdots & \ddots & \vdots \\ x_M(t_1) & \dots & x_M(t_K) \end{bmatrix} + \begin{bmatrix} e_0(t_1) & \dots & e_0(t_K) \\ \vdots & \ddots & \vdots \\ e_{N-1}(t_1) & \dots & e_{N-1}(t_K) \end{bmatrix} \end{aligned} \tag{2.10}$$

where the final measured data is the $y(t) \in \mathbb{C}^{N\times K}$.

2.4.1 Covariance matrix model and subspaces

It can be assumed that the noise can be approximated as zero mean, complex white Gaussian noise with a variance σ^2. To simplify the expressions, the time indices may also be removed. With the signal model as in Section 2.4, where an element in the array matrix is denoted $y_n = \sum_{m=1}^{M} x_m e^{in\Delta\varphi_m} + e_n,\ n \in [0, N-1]$, the l, j:th element in (2.10) of the covariance

$R_y = E\{yy^H\}$ of the array model would be

$$(R_y)_{l,j} = E\{y_l y_j^H\} = E\left\{ \left[\sum_{m=1}^{M} (x_m e^{li\Delta\varphi_m}) + e_l \right] \left[\sum_{p=1}^{M} (x_p^H e^{-ji\Delta\varphi_p}) + e_j \right] \right\} =$$
$$E\left\{ \left[\sum_{m=1}^{M} x_m e^{li\Delta\varphi_m} \right] \left[\sum_{p=1}^{M} x_p^H e^{-ji\Delta\varphi_p} \right] \right\} + \sigma^2\delta_{l,j} = \sum_{m=1}^{M}\sum_{p=1}^{M} E\{x_m x_p^H\}_{l,j} e^{li\Delta\varphi_m} e^{-ji\Delta\varphi_p} + \sigma^2\delta_{l,j} \quad .$$
$$= \sum_{m=1}^{M}\sum_{p=1}^{M} (R_x)_{l,j} e^{li\Delta\varphi_m} e^{-ji\Delta\varphi_p} + \sigma^2\delta_{l,j} \tag{2.11}$$

The signals are also assumed to be uncorrelated so that $(R_x)_{m,p} = E\{x_m x_p\} = 0; m \neq p$. R_x is therefore a diagonal matrix whose elements correspond to the signal strengths. Here the exponential and the sums over indices m and p respectively can be identified as the Vandermonde matrix A, and its Hermitian, A^H. It can therefore be shown that the covariance of the array model is

$$R_y = AR_xA^H + \sigma^2 I \tag{2.12}$$

and this therefore contains all information about the DOAs of the signals. Given that the number of signals M is known, this property of R is utilized to create the signal subspace. Performing an eigen decomposition of the covariance matrix, the following is achieved

$$R_y = V\Lambda V^{-1} = V\Lambda V^H \tag{2.13}$$

where the eigenvalues λ_i are elements in the diagonal matrix Λ, arranged in descending order. In equation (2.13) the equality $V^{-1} = V^H$ is a consequence from the possibility to prove that R_y is an Hermitian matrix. By comparing this to (2.12), it is possible to select the M first columns of V to span the signal subspace U_s and the remaining $N-M$ columns and eigenvalues to represent the noise subspace U_n and the noise variance σ^2, respectively. The signal subspace U_s, can therefore be described as an estimate of the Vandermonde steering matrix A, multiplied with a square matrix C, whose elements correspond to the signal strengths and noise.

2.4.2 Signal environment

Whether an SSR system can detect the presence of a signal to process and decode it is entirely dependent on what environment the signal exists in. The main contributions to the environment are noise and other signals that interfere with the signal of interest (SOI). If a relatively weak SOI exists in a very noisy environment with many strong interfering signals, it is naturally difficult to decode the SOI.

One significant part of the signal environment is noise. Noise is inevitable when performing radar measurements and can have many sources. The noise sources may include other communications, hardware such as mixers and amplifiers, and background radiation from the universe. All of these noise sources account for different types of noise, but a common way to describe the noise in a received signal is as "complex white Gaussian noise". Complex white Gaussian noise can be modeled as random complex variables with a normal distribution and equal intensity at all frequencies. The noise mean is zero and has a finite variance σ^2. When studying noise, its power is rarely relevant on its own, but rather in relation to the power of the

signals. Therefore, a common property to study is the Signal-to-Noise Ratio (SNR) [10], which is defined as the ratio of the power from a signal and the noise. Because of the magnitude of this ratio, it is often expressed in decibels as

$$\mathrm{SNR}|_{\mathrm{dB}} = 10\log\left|\frac{P_{\mathrm{signal}}}{P_{\mathrm{noise}}}\right| = 10\log\left|\frac{A_{\mathrm{signal}}}{A_{\mathrm{noise}}}\right|^2 \tag{2.14}$$

where A is the electromagnetic field amplitude in V/m quadratically proportional to the power as $P \propto A^2$. To distinguish a signal from the noise, a high SNR is desirable.

In the SSR application, a prominent part of the signal environment is interfering signals. Because these in many cases are very similar to the SOIs, they can easily be misinterpreted as parts of an SOI. While many methods exist to distinguish signals from each other, there exist none that completely solves this problem. In many cases, to characterize the level of interfering signals in an environment, a property called the Signal-to-Interfering-Ratio (SIR) is used. Similar to the SNR in (2.14), this is made up of a quota between the power of the SOI and the interfering signals as

$$\mathrm{SIR}|_{\mathrm{dB}} = 10\log\left|\frac{P_{\mathrm{SOI}}}{P_{\mathrm{interf}}}\right| = 10\log\left|\frac{A_{\mathrm{SOI}}}{A_{\mathrm{interf}}}\right|^2. \tag{2.15}$$

In contrast to the SNR where all noise sources are mixed up, one SOI can have many SIRs to relate it to several interfering signals. It is also possible to create an SIR ratio for the environment where interfering signals are allowed to positively interfere with each other. For the purpose of this thesis however, the SIR for the SOI in relation to the individual interfering signal causing the lowest, and therefore worst, SIR is used.

A required minimum SIR value is commonly used as a metric to describe how sensitive a system is to interfering signals. It states that if an SOI has a SIR $\geq \mathrm{SIR}_{\mathrm{min}}$ it is possible to distinguish the SOI from the interfering signals, and therefore also decode the signal.

2.5 Direction of arrival estimation algorithms

The fundamental problem in DOA estimations is to determine the array phases caused by the plane waves arriving to the array as explained in Section 2.3.1. These phases are easy to translate into DOAs by (2.8). There exists many algorithms to find frequencies in signals which can be used for this purpose, some of these algorithms are explained below.

2.5.1 Monopulse algorithm

There are two versions of the monopulse algorithm, in this thesis the phase monopulse is used. For the phase monopulse algorithm, an analog SSR architecture as in Figure 2.5 is sufficient. With this, the antenna is steered in a direction θ_0 by introducing a phase shift in the feed of each element as done in (2.3), creating a Vandermonde steering vector for the array elements. The monopulse algorithm then divides the ULA into two equal sections, a right and a left side, where the elements are summed up. It then adds or subtracts the two sides, to create a sum, Σ, and a delta, Δ, channels as in Figure 2.5. This means that the final sum and delta channels

is

$$
\begin{aligned}
y_\Sigma(t) &= \sum_{n=1}^{N} y_n(t) \\
y_\Delta(t) &= \sum_{n=1}^{N} y_n(t) H(n) \\
H(n) &= \begin{cases} 1 & n \leq N/2 \\ -1 & n > N/2 \end{cases}, \quad 2|N.
\end{aligned}
\tag{2.16}
$$

These channels create a sum and delta lobe in the directional gain in the azimuth plane where the sum lobe is centered at the steering direction θ_0 and the delta lobe has a null in θ_0. An example of how this directional gain pattern might look like is seen in Figure 2.8 where the lobes are steered in a direction $\theta_0 = 30°$.

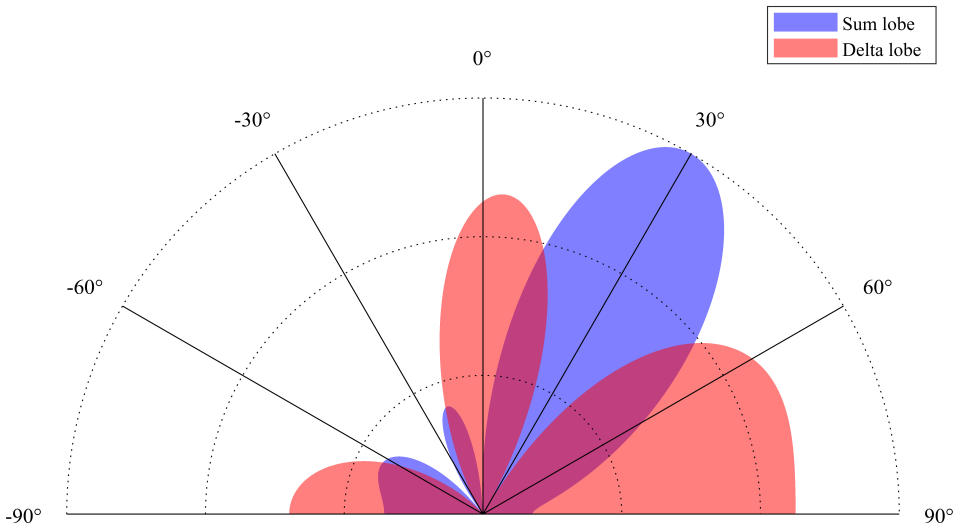

Figure 2.8: An example of directional gain of the sum and delta lobes. Lobes are steered in $\theta_0 = 30°$. The sum lobe is centered in θ_0 and the delta lobe has a null in θ_0.

Considering two channels from each half of a ULA, the sum and delta channels can be described as the dot product of the two channels with $\begin{bmatrix} 1 & 1 \end{bmatrix}$ or $\begin{bmatrix} 1 & -1 \end{bmatrix}$. The individual elements are separated by a phase shift caused by the signal's DOA, θ, as $\Delta\varphi = \frac{2\pi d}{\lambda}(\sin\theta - \sin\theta_0)$ where θ_0 is the direction the array is steered to. This means that the array experiences phases as

$$
\begin{bmatrix} 0 & \Delta\varphi & \dots & (N-1)\Delta\varphi \end{bmatrix}, \quad 2|N \tag{2.17}
$$

at each element. By dividing the array into a left and right part with an equal number of elements, numbering the elements in each half starting from the same direction, the elements in the same respective positions of each half experience a phase difference $\frac{N}{2}\Delta\varphi$. Because of this, it is possible to describe a signal $s(t)$ arriving to the array in the sum and delta channels as shifted in phase by $\frac{N}{2}\Delta\varphi$, so that

$$
\begin{aligned}
y_\Sigma(t) &= (1 + e^{-i\frac{N}{2}\Delta\varphi}) s(t) \\
y_\Delta(t) &= (1 - e^{-i\frac{N}{2}\Delta\varphi}) s(t)
\end{aligned}
\tag{2.18}
$$

where the imaginary part of the quota of these is the monopulse angle

$$\Psi = \operatorname{Im}\left\{\frac{y_\Delta(t)}{y_\Sigma(t)}\right\} = \operatorname{Im}\left\{\frac{1-e^{-i\frac{N}{2}\varphi}}{1+e^{-i\frac{N}{2}\varphi}}\right\} = \operatorname{Im}\left\{\frac{e^{i\frac{N}{2}\frac{\varphi}{2}}-e^{-i\frac{N}{2}\frac{\varphi}{2}}}{e^{i\frac{N}{2}\frac{\varphi}{2}}+e^{-i\frac{N}{2}\frac{\varphi}{2}}}\right\} = \operatorname{Im}\left\{\frac{i\sin\frac{N}{2}\frac{\varphi}{2}}{\cos\frac{N}{2}\frac{\varphi}{2}}\right\} = \tan\frac{N}{2}\frac{\varphi}{2}. \tag{2.19}$$

Here it is possible to solve for θ as

$$\begin{aligned}\arctan\Psi =& \frac{N}{4}\frac{2\pi d_a}{\lambda}\left(\sin\theta - \sin\theta_0\right)\\ \theta =& \arcsin\left(\frac{2\lambda}{N\pi d_a}\arctan(\Psi) + \sin\theta_0\right).\end{aligned} \tag{2.20}$$

In practice, to form an estimate of the monopulse angle from a sampled signal, a mean is made from the samples from these two channels. The estimate of the monopulse angle $\hat{\Psi}$ can then be estimated from the samples $y(t_k)$ as

$$\hat{\Psi}(\theta) = \frac{1}{K}\sum_{k=1}^{K}\operatorname{Im}\left\{\frac{y_\Delta(t_k)}{y_\Sigma(t_k)}\right\}. \tag{2.21}$$

which in turn yields a DOA estimate as

$$\hat{\theta} = \arcsin\left(\frac{2\lambda}{N\pi d_a}\arctan\hat{\Psi} + \sin\theta_0\right). \tag{2.22}$$

It can be noted that the monopulse algorithm only provides one estimated DOA for each measurement, no matter how many signals there are in the samples where the measurement is performed.

2.5.2 ESPRIT

Estimation of Signal Parameters via Rotational Invariance Techniques (ESPRIT) is an algorithm that utilizes the signal subspace derived in Section 2.4.1 to find how parts of the subspace are related to each other [11, ch. 4.7, pp. 166-167], [8, Ch 9.3.4]. To derive it, the Vandermonde steering matrix A is divided into two parts by selection matrices J_1 and J_2 as

$$\begin{aligned}A_1 = J_1 A = \begin{bmatrix} I_{M-1} & 0\end{bmatrix} U_s\\ A_2 = J_2 A = \begin{bmatrix} 0 & I_{M-1}\end{bmatrix} U_s.\end{aligned} \tag{2.23}$$

Where the signal subspace is assumed to be of size It is observed that the two partitions hold the following relation

$$\begin{aligned}A_2 &= A_1 T\\ T &= \begin{bmatrix} e^{-i\varphi_1} & \dots & 0\\ \vdots & \ddots & \vdots\\ 0 & \dots & e^{-i\varphi_M}\end{bmatrix},\end{aligned} \tag{2.24}$$

meaning that the multiplication of A_1 with T is a rotation. In a similar way, the signal subspace can also be divided into two parts by the same selection matrices as

$$\begin{aligned} U_{s1} &= J_1 U_s = \begin{bmatrix} I_{M-1} & 0 \end{bmatrix} U_s \\ U_{s2} &= J_2 U_s = \begin{bmatrix} 0 & I_{M-1} \end{bmatrix} U_s \end{aligned} \tag{2.25}$$

where it can be shown that $U_s = AC$, where $C \in \mathbb{C}^{M \times M}$ is a non-singular matrix since the columns of A should span the signal subspace. From this it is possible to express the relation of the signal subspaces as

$$\begin{aligned} U_{s2} = A_2 C = A_1 T C = U_{s1} C^{-1} T C = U_{s1} \Phi \\ \Phi = C^{-1} T C. \end{aligned} \tag{2.26}$$

Where it is possible to solve for Φ using the subspaces as

$$\begin{aligned} U_{s2} = U_{s1} \Phi \\ \Phi = (U_{s1}^H U_{s1})^{-1} U_{s1}^H U_{s2}. \end{aligned} \tag{2.27}$$

By instead using estimates of the signal subspace $\hat{U}_s$ to calculate $\hat{\Phi} = (\hat{U}_{s1}^H \hat{U}_{s1})^{-1} \hat{U}_{s1}^H \hat{U}_{s2}$, an eigenvalue decomposition can be made to find an estimation $\hat{T}$. Where the estimates of the array phases are the phases of the eigenvalues of $\hat{\Phi}$ according to

$$\hat{\Phi} = \hat{C}^{-1} \hat{T} \hat{C} = \hat{C}^{-1} \begin{bmatrix} e^{-i\hat{\varphi}_1} & \dots & 0 \\ \vdots & \ddots & \vdots \\ 0 & \dots & e^{-i\hat{\varphi}_M} \end{bmatrix} \hat{C}. \tag{2.28}$$

The estimated array phases $\{\hat{\varphi}_m\}_{m=1}^M$ give the DOA estimations $\{\hat{\theta}_m\}_{m=1}^M$ when used in equation (2.8).

The selection matrices used in ESPRIT are not unique and several other versions of the matrices exist. The only requirement is that (2.24) is fulfilled.

2.5.3 MUSIC

Multiple Signal Classification (MUSIC) is an algorithm that utilizes the noise subspace [11, Ch. 4.5, pp. 159-164] [8, Ch. 9.3.2], U_n, described in Section 2.4.1. The noise subspace is the orthogonal complement to the signal space and since the noise fills the whole space it is a subspace of the noise space. Therefore, the Vandermonde steering vectors should lie in the null space of the noise subspace. This implies that

$$\begin{aligned} A^H U_n = 0 \\ \Rightarrow \\ a^H(\theta_m) U_n = 0 \ \ \forall m. \end{aligned} \tag{2.29}$$

Taking the norm of this, an equation can be constructed as

$$|a^H(\theta) U_n|^2 = a^H(\theta) U_n (a^H(\theta) U_n)^H = a^H(\theta) U_n U_n^H a(\theta) = 0 \tag{2.30}$$

where $a^H(\theta)U_nU_n^Ha(\theta) \in \mathbb{C}$ is a scalar. It is possible to form a polynomial from this by letting the Vandermonde vectors be described as functions of a complex variable $z = \alpha e^{i\varphi}$ where $\alpha \in \mathbb{R}$ is arbitrary, so that $a(z) = \begin{bmatrix}1 & z^1 & \dots & z^{N-1}\end{bmatrix}$. This yields that

$$\begin{gathered} a^T(z^{-1})U_nU_n^Ha(z) = 0 \\ \Leftrightarrow \\ \sum_{j=0}^{N-1}\sum_{l=0}^{N-1} z^{j-l}(U_nU_n^H)_{lj} = 0 \end{gathered} \tag{2.31}$$

whose roots are $\{z_i\}_{-N+1}^{N-1}$. The M roots closest to the unit circle in the complex plane carry the array phases as arguments $\varphi_m = \angle z_m$. These phases can be used in (2.8) to find the DOA estimates $\{\hat{\theta}_m\}_{m=1}^M$.

This version, which is used in this thesis, is called Root MUSIC because it finds the roots of a polynomial, but there are other versions. Another common version of MUSIC instead constructs a spectrum of the noise subspace to identify the position of spectral lines.

2.5.4 Higher Order Yule-Walker algorithm

The Higher-Order Yule-Walker (HOYW) algorithm [11, Ch. 4.4, pp. 155 - 159], utilizes a slightly different model than the covariance model explained in Section 2.4.1. Here it is assumed that there exists an annihilating factor for each signal $x_m(t)$ with array phases φ_m, so that

$$(1 - z^{-1}e^{i\varphi_m})x_m(t) = 0. \tag{2.32}$$

From this, a polynomial can be created as

$$\begin{gathered} B(z) = \prod_{m=1}^{M}(1 - z^{-1}e^{i\varphi_m}) = 1 + \sum_{m=1}^{M} b_k m^{-m} \\ \Rightarrow \\ B(z)\sum_{m=1}^{M} x(t) = 0 \end{gathered} \tag{2.33}$$

where z^{-1} is a delay operator, which shifts a time vector one step in time. It can be seen that the roots of this polynomial hold information of the array phases. For a sampled signal with noise, $y(t) = x(t) + e(t)$, where $x(t)$ is already multiplied with the steering matrix A to simplify notation, this can be expressed as

$$\begin{gathered} B(z)y(t) = B(z)(x(t) + e(t)) = B(z)e(t) \\ y(t_k) + b_1y(t_{k-1}) + \cdots + b_My(t_{k-M}) = e(t_k) + b_1(t_{k-1}) + \cdots + b_Me(t_{k-M}) \end{gathered} \tag{2.34}$$

This can in vector form be written as

$$\begin{bmatrix}y(t_k) & \dots & y(t_{k-M})\end{bmatrix}\begin{bmatrix}1 \\ \vec{b}\end{bmatrix} = e(t_k) + b_1(t_{k-1}) + \cdots + b_Me(t_{k-M}) \tag{2.35}$$

where $\vec{b} = \begin{bmatrix} b_1 & \dots & b_M \end{bmatrix}^T$. This could be pre-multiplied by the same signal vector shifted by M samples to form

$$\begin{bmatrix} y(t_{k-M-1}) \\ \dots \\ y(t_{k-M-M}) \end{bmatrix} \begin{bmatrix} y^H(t) & \dots & y^H(t_{k-M}) \end{bmatrix} \begin{bmatrix} 1 \\ \vec{b} \end{bmatrix} = \begin{bmatrix} e(t_k) \\ \dots \\ e(t_{k-M}) \end{bmatrix} \begin{bmatrix} 1 \\ \vec{b} \end{bmatrix} \tag{2.36}$$

where the expectation value can be taken to get rid of the noise, since it is zero mean. A matrix Γ can also be introduced as the expectation value of the differently shifted signal samples. This leaves

$$\begin{aligned} E\left\{ \begin{bmatrix} y(t_{k-M-1}) \\ \dots \\ y(t_{k-M-M}) \end{bmatrix} \begin{bmatrix} y^H(t_k) & \dots & y^H(t_{k-M}) \end{bmatrix} \right\} \begin{bmatrix} 1 \\ \vec{b} \end{bmatrix} &= E\left\{ \begin{bmatrix} e(t_k) \\ \dots \\ e(t_{k-M}) \end{bmatrix} \right\} \begin{bmatrix} 1 \\ \vec{b} \end{bmatrix} \\ \Gamma \begin{bmatrix} 1 \\ \vec{b} \end{bmatrix} &= 0 \end{aligned} \tag{2.37}$$

By rewriting this as

$$\Omega\vec{b} = -r \tag{2.38}$$

where r is the first row of Γ and Ω are the remaining rows. Because $B(z)$ annihilates the array phase components of $x(t)$, its M roots closest to the unit circle, z_m, have the property $\angle z_m = \varphi_m$. This makes it possible to gather the DOAs of the signals.

When using measurements to construct an estimate $\hat{\Gamma}$ in practice, this problem may become ill-conditioned. To still make estimates, a singular value decomposition is made of $\hat{\Omega}$ as

$$\hat{\Omega} = \begin{bmatrix} U_s & U_n \end{bmatrix} \begin{bmatrix} \Sigma_s & 0 \\ 0 & \Sigma_n \end{bmatrix} \begin{bmatrix} V_s^H \\ V_n^H \end{bmatrix} \tag{2.39}$$

where the signal subspace appear as U_s. By simply using the components of the singular value decomposition belonging to the signal subspace, a Moore-Penrose inverse can be used to solve for the polynomial coefficients as

$$\hat{b} = -V_s\Sigma_s^{-1}U_s^H\hat{r}. \tag{2.40}$$

The DOA estimates are found as the the phases $\angle\hat{z}_m = \hat{\varphi}_m$.

A more general case of this algorithm is explained further in [11, Ch. 4.4, pp. 155-159].

2.6 Signal processing chain

A traditional interrogator that applies the monopulse algorithm in an analog architecture has a rather straightforward signal processing chain. When a reply is detected in a continuous stream of measured samples, it is decoded with some techniques utilizing the PPM modulation scheme. All samples in the time window for the signal of interest (SOI) are then studied to remove samples that are too disturbed or simply do not contain any pulse of the signal. From the good samples that are left, a DOA estimation is performed to produce an estimate that is paired with the decoded signal's information.

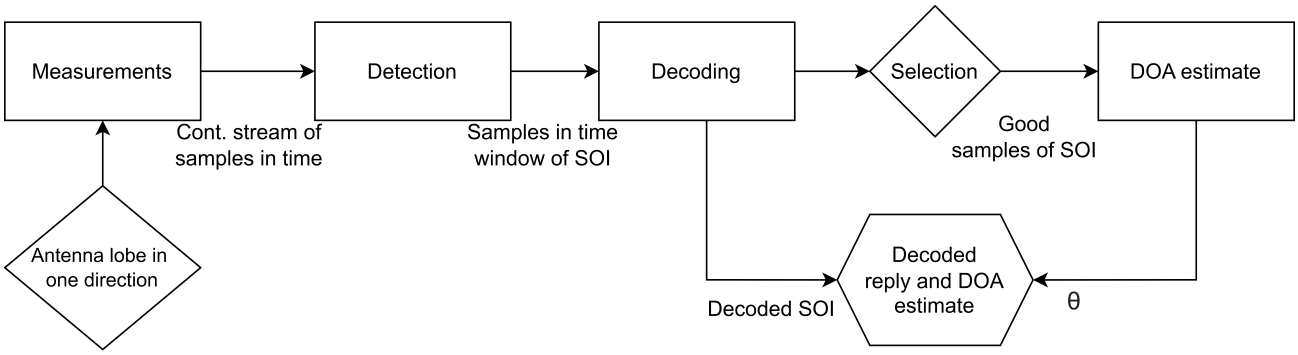

Figure 2.9: A description of the analog signal processing chain. A reply is detected and decoded before the good samples of an SOI, which are not as disturbed by interfering signals, are used in a DOA estimate algorithm. The result is a decoded signal and a DOA.

With this approach illustrated in Figure 2.9, one signal is decoded and an algorithm is used to produce one DOA estimate for this signal. In this case it is important to bear in mind that the measurements are performed one array steering direction, θ_0, at a time. This means that the SOI needs to be within the main lobe steered at θ_0. Otherwise, the antenna does not see the SOI. This also means that if an interfering signal lies within the steered array lobe, it disturbs the measurement of the SOI. This could lead to one of two outcomes: either the measurement is completely ruined by the interfering signal if it renders no undisturbed samples of the SOI, or it makes the measurement biased towards the interfering signal's DOA since the estimate is based on samples containing this DOA as well.

For the digital architecture shown in Figure 2.6, no examples of how the signal processing chain could be implemented in an interrogator have been found in literature. In this thesis, the implementation in Figure 2.10 has been proposed and analyzed. While it is not known if it is plausible regarding hardware requirements and precision, the logic holds and it could therefore be a possible way of integrating the digital architecture algorithms described in Sections 2.5.2, 2.5.3 and 2.5.4.

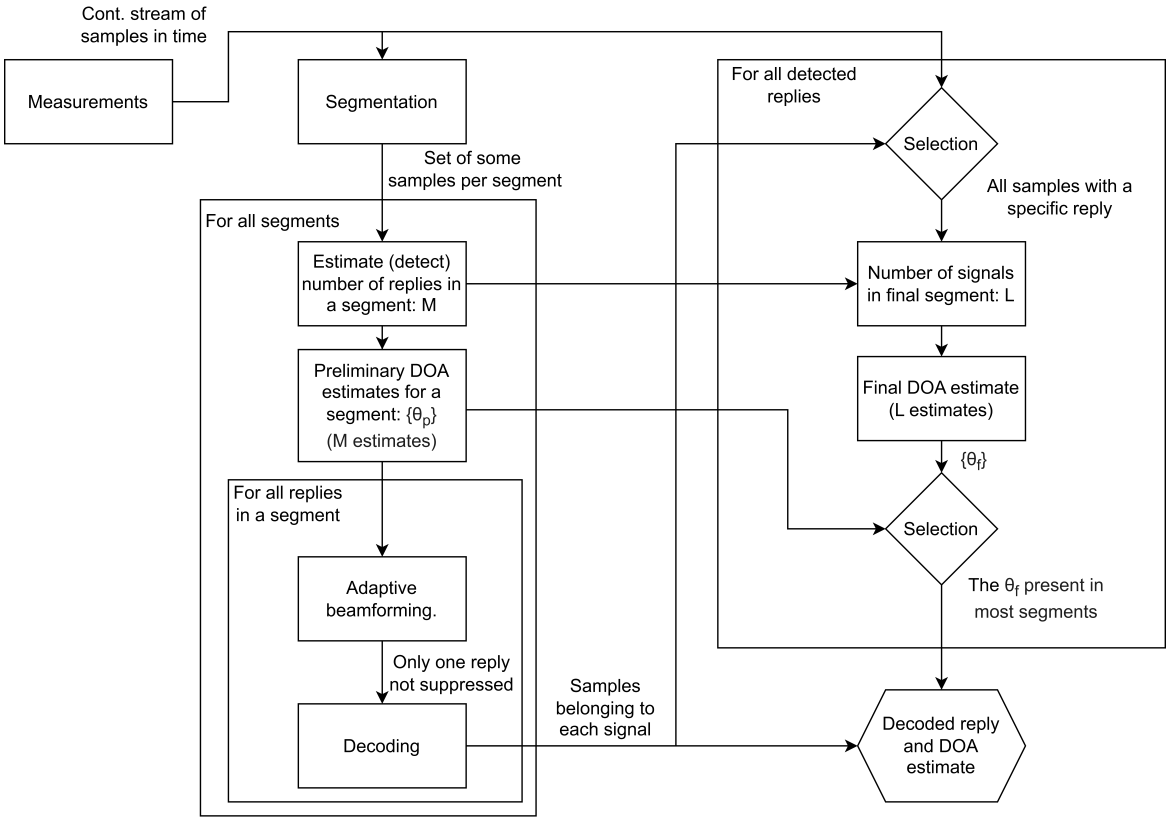

Figure 2.10: Proposed signal processing chain for a digital SSR architecture. The continuous stream of samples is first split up in segments that are processed. In each segment the number of signals is estimated and a preliminary DOA estimation is made. For each signal in the segment, adaptive beamforming is performed to suppress all other signals. The remaining signal is then decoded. One at a time, all of these decoded signals are individually considered as SOIs with all the samples they consist of. Another DOA estimation is made on these samples for each SOI. The DOA that was present in all segments of this SOI is assumed to belong to the SOI and is paired with the decoded SOI.

One factor causing the architecture in Figure 2.10 to seem more complicated, is that the digital algorithms produce more estimates for each measurement. Consequently, additional processing is required to determine how the DOA estimates should be paired with the signals. The digital algorithms also require prior knowledge of how many DOAs they should estimate in a measurement. This can be done through many different ways, mainly searching for preambles and pulses or by so-called model order selection algorithms [12].

When the number of signals in each segment is known, the digital algorithms can be applied. Using these estimated DOAs to apply beamforming that suppresses all but one desired signal, an SOI, the probability of decoding is increased [5]. This means that it is more likely to detect and decode the signals one at a time. When the signals are decoded, it is possible to treat each signal as an SOI one at a time and only select the time window and samples which that SOI covers, setting the remaining samples in the time window to zero. It is also possible to completely remove all samples that do not contain any pulses of the SOI. With the remaining samples together with the information about the other interfering signals, it would be possible to determine the number of interfering signals in the new time window. A final DOA estimation

could then be done, where the resulting estimates could be compared to the preliminary DOA estimates from all segments that the SOI covered. Since the probability for an interfering signal to completely overlap an SOI in time is very low, the SOIs DOA should be the one closest to the preliminary DOAs that were estimated from the segments covered by the SOI.

2.7 Statistics

In simulations, statistical ways of describing random events are crucial. When certain events are not possible to determine beforehand, using a random variable could create a realistic event to e.g. simulate a measurement. When enough simulations are made, the simulation should approach how a real measurement should behave. If a simulation has done this, it is said that the simulation has converged, and the measurements of the simulations should represent the probability distribution of measurement results from a real-life scenario.

To generate random variables, they are often selected from different distributions, which represent what values a random variable should converge to if enough samples of the variable are taken. One common example is the uniform distribution, which simply gives a variable equal probability of being any value within a certain interval. Another common distribution is the Poisson distribution. A random variable X that is Poisson distributed follows the probability distribution

$$\mathbf{P}(X = k) = \frac{\lambda^k e^{-\lambda}}{k!} \tag{2.41}$$

where the integer k is the value of the variable and λ is the expected value of X. The expected value is given by $\lambda = \mathbf{E}\{X\} = \sum_{k=1}^{\infty} k\mathbf{P}(X = k)$ where $\{X_g\}$ is the set of possible values of X. Poisson distributions accurately describe the probability of independent events occurring in time, making it well suited to describe the number of interfering signals occurring in a set time frame.

A common way to statistically describe measurements of a quantity is with the mean bias error and the standard deviation. The mean bias error is simply how accurate or biased a measurement is towards any value. An estimate of the standard deviation can be calculated by subtracting the true value of a variable from the sample mean as

$$e_{\text{bias}} = \frac{1}{T-1}\sum_{t=1}^{T} \hat{x}_t - x_{\text{true}} \tag{2.42}$$

where there are T measurements $\hat{x}$ and x_{true} is the true value for the measurement. This gives a view of how accurate the measurements are. Standard deviation however, describes how consistent or precise the measurements are. It is calculated as the square of all deviations from the mean

$$\sigma = \sqrt{\frac{1}{T-1}\sum_{t=1}^{T} |\hat{x}_t - \mu|^2} \tag{2.43}$$

where μ is the sample mean of all measured variables. The precision is calculated as the inverse of this

$$\text{Precision} = \frac{1}{\sigma^2}. \tag{2.44}$$

3
Methods

The method to test the DOA algorithms have been simulations. In this chapter, the simulation set-up is described, as well as how and why assumptions have been made.

3.1 Antenna model

A ULA with $N = 6$ elements spaced by $d_a = 10\,\text{cm}$ was assumed for the simulations. This model avoids grating lobes, since the element spacing is less than half the wavelength. By conventional beamforming it is also possible to steer the main lobe of the array. This antenna model is then capable of covering the entire space in front of the array by scanning in a few steering directions.

The antenna elements in the array were not assumed to be ideal isotopically radiating. Because of the few elements in the array and the big sector to cover, the elements were assumed to have rather wide main lobes that could cover most of the sector with a relatively uniform directional gain. The elements directional gain pattern was therefore selected as

$$G(\theta) = \cos^2\left(\frac{\theta}{2}\right) \tag{3.1}$$

which fulfills this rather well, and is claimed to be a good approximation of the directional gain of a single element [7, p.52]. Its full 3 dB-width becomes 180°, meaning that it covers the entire azimuth sector in front of the array.

3.2 Environment

The simulations were primarily characterized by the created environments. The environments were characterized by the intensity of interfering signals that were present during the simulation time window, and by how far away from the antenna array the Signal Of Interest (SOI) source was placed.

The number of interfering signals that appeared in the simulated time window was determined by a Poisson distribution as described in Section 2.7. To calculate the intensities λ of the Poisson distributions, the number of transponders in an airspace was considered. By studying different areas of live flight maps such as Flightradar24 [13], four amounts of transponders, T, were selected within an $R = 1100\,\text{km}$ radius as $T = 100$, 250, 500 or 1000. It was then determined from ICAO [6, p. 3-70] that the minimum reply rate all transponders have is 50 replies per second. Assuming that most transponders are capable of replying at least twice

as fast, each transponder could then reply at $f_{\text{reply}} = 100$ replies per second. From this, the intensity per time and area can be calculated as

$$\gamma = \frac{T f_{\text{reply}}}{\pi R^2}. \tag{3.2}$$

By multiplying γ with the area where interfering signals were placed A_{interf}, and the time window where any other signal would interfere with the SOI, the Poisson intensity could be calculated as $\lambda = 2\gamma t_{\text{long}} A_{\text{interf}}$ where $t_{long} = 1\,\mu\text{s}$ is the length of a Mode S long reply which the SOI always is. The factor of two in the expression for λ comes from the fact that an interfering long reply overlaps with the SOI if it starts $< t_{\text{long}}$ before the SOI. The resulting intensities are shown in Table 3.1.

Table 3.1: Interfering occurrence intensities per area and time.

Observed # aircraft	100	250	500	1000
Occurrence intensity $\gamma[1/\text{km}^2\text{s}]$	0.0026	0.0066	0.013	0.026
Expected number of interfering replies λ during (during long SOI)	1.176	2.986	5.881	11.726

Another case with zero observed aircraft was also included to set a reference of how the algorithms might perform without interfering signals.

In ICAO [6, p. 3-70] the ratio between the number of short and long replies a transponder may transmit is discussed. In general, it is specified that short replies should be more common compared to long replies. Therefore, each occurrence of an interfering signal was given a 60% probability of being a short reply and a 40% probability of being a long reply.

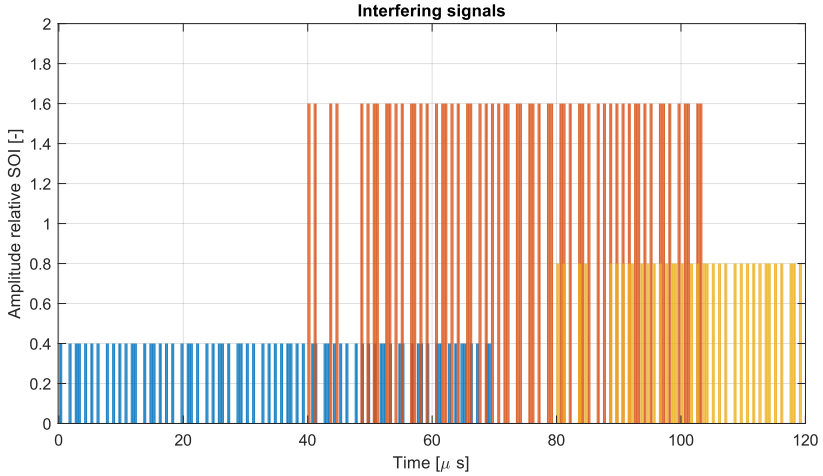

Figure 3.1: Example with three interfering signals placed with different amplitudes and starting times. Shown during a long reply time window.

All interfering signals were randomly placed in an area in front of the array within a range of $R_{\text{LoS}} = 1100\,\text{km}$ and a minimum range of 100 km and their starting times were randomized in

an interval from 120 µs before the start of the SOI to the end of the SOI. This was done since a long reply that started < 120 µs before the SOI would overlap with the SOI. This also meant that a short reply that started earlier than 64 µs before the SOI, would not interfere with the SOI in the simulation, any such replies were therefore removed. However, this was accounted for when the intensity of occurrences of interfering signals was selected. A final simulated time window without an SOI might look as depicted in Figure 3.1.

3.3 Signals

The signal model in Section 2.4 was used as a foundation to model the signals that arrived at the ULA. To model a realistic implementation and array, however, some features of the (2.10) were adjusted. To begin with, since the mode S carrier frequency is allowed in the range $[1089, 1091]$MHz, the wavelength in the phase differences from (2.8) would be altered to the specific randomized wavelength in of the signal so that

$$\Delta\varphi_m(\theta_m, f_m) = \frac{2\pi d_a \sin\theta_{\text{DOA},m}}{\lambda_m} = \frac{f_m}{c} 2\pi d_a \sin\theta_{\text{DOA},m} \tag{3.3}$$

in the steering vectors $a(\theta_m, f_m)$. When the signal is assumed to be mixed down to baseband, this deviation from 1090 MHz means that the signal would still have a frequency in the range $[-1, 1]$ MHz. Therefore, the signal $x_m(t)$ would be placed on a complex envelope so that a signal would be $x'(t_k) = x(t_k)e^{2\pi i t_k f + i\psi}$ where $\psi \in [0, 2\pi]$ is a randomized phase constant and $f \in [-1, 1]$ MHz is a randomized frequency.

Another adjustment to (2.10) was that the antenna element directional gain was included so that the steering vectors in the steering matrix were multiplied with the element directional gain for the directions. The steering matrix then consisted of elements as $\cos^2(\theta_m/2)a_n(\theta_m, f_m) = \cos^2(\theta_m/2)e^{ni\Delta\varphi_m(\theta_m, f_m)}$. In total, the modified signal model became

$$\begin{aligned} y'(t) =& A'\vec{x'}(t) + \vec{e}(t) = \\ &\left[\cos^2\left(\tfrac{\theta_1}{2}\right)\vec{a}(\theta_1, f_1) \quad \dots \quad \cos^2\left(\tfrac{\theta_M}{2}\right)\vec{a}(\theta_M, f_M)\right] \begin{bmatrix} x_1(t_1)e^{it_1 f_1 + i\psi_1} & \dots & x_1(t_K)e^{it_K f_1 + i\psi_1} \\ \vdots & \ddots & \vdots \\ x_M(t_1)e^{it_1 f_M + i\psi_M} & \dots & x_M(t_K)e^{it_K f_M + i\psi_M} \end{bmatrix} + \vec{e}(t) \end{aligned} \tag{3.4}$$

where the noise remained the same complex white gaussian noise as described in Section 2.4.

3.4 Simulation

The simulations were performed in MATLAB. MATLAB was selected since it is a matrix-based language which made it suitable for the algorithms that heavily rely on linear algebra and matrix operations. To reuse certain code and reduce simulation sizes, the simulations were divided into two main parts. First, the creation of the environments without any SOI, and then the addition of the SOI on the Mode S long format, together with the DOA estimations. This allowed for simulated environments to be reused for all algorithms, ensuring that all algorithms were tested in the same scenarios. This also made large parts of the code reusable, and reduced

the computational time.

It was assumed that the decoding of the signals was already completed and that the length of the signal could be determined. Therefore, the time window to perform the simulation on could be matched to the SOI. This meant that with the SOI as a mode S long reply, the simulation time window would be 120 µs long. The time window sampling interval was set to 0.1 µs. If the radar is assumed to use a quadrature demodulator, which is the modern approach, this would be approximately the Nyquist frequency required to sample the signal without aliasing. However, no actual sampling at 1090 MHz is performed in the simulations, so there is no requirement to adhere to the Nyquist theorem perfectly. This, however, gives a realistic value.

The number of interfering signals for each environment was picked from a random distribution with one of the four intensities presented in Table 3.1. Their azimuth angles were selected uniformly distributed in front of the array from $-90°$ to $90°$. The maximum limit for the simulated ranges was decided by the line of sight range for an aircraft described in AppendixA.2. With an interrogator on an aircraft at an altitude of $h = 15\,\text{km}$, the line of sight range was $R_{\text{los}} = 1010\,\text{km}$, which was rounded up to $R_{\text{max}} = 1100\,\text{km}$ since more favorable weather conditions would allow further line of sight than calculated in (A.2). Another minimum range limit was also used as $R_{\text{min}} = 100\,\text{km}$. This range was used since aircraft would keep appropriate distance to each other. The distance to the interfering signals was randomized as in (A.5) to make the distribution uniform across the entire area.

When the positions of interfering signals were determined, the signals were randomized on the mode S format. All transponders were assumed to transmit with the same power. Hence the range determined the amplitude arriving at the receiving antenna as

$$A_{\text{array}} = \frac{\lambda}{4\pi R} A_0 \tag{3.5}$$

for propagation of a distance R to the array, where A_0 is the original radiated amplitude which was assumed to be unity since all transponders were assumed to radiate the same amount of power. The signal was then applied to the array as in (3.4) before the nosie $e(t)$ was added. The noise was set to complex white Gaussian noise with an amplitude equivalent to a transponder amplitude at a range of 2500 km. This meant that the SNR would entirely be determined by the distance to the transponders. For the SOIs, the ranges 300 km, 600 km and 900 km meant a DOA in boresight ($\theta = 0$) had an SNR of 18 dB, 12 dB and 9 dB respectively. However, the SNR decreased for larger DOAs since the directional gain of the antenna elements decreased. For example at 45°, the SNR was 1.3 dB lower than in boresight. However, the SNR never goes below 4.3 dB since at 80°, the directional gain is $20 \log \cos^2 \frac{80°}{2} = -4.6\,\text{dB}$.

While interfering signals are assumed to appear in the full space in front of the array, SOIs were only simulated for positive DOAs. This is because of symmetry. Furthermore, the SOIs were not simulated for DOAs greater than 80°. This was because beyond this point the errors naturally become very large as explained in Appendix A.1. In practical applications these angles would be covered by another antenna. To reduce the computing power needed for the simulations, the SOI DOAs were spaced evenly with 0.5° between each other in the $[0°, 80°]$ range.

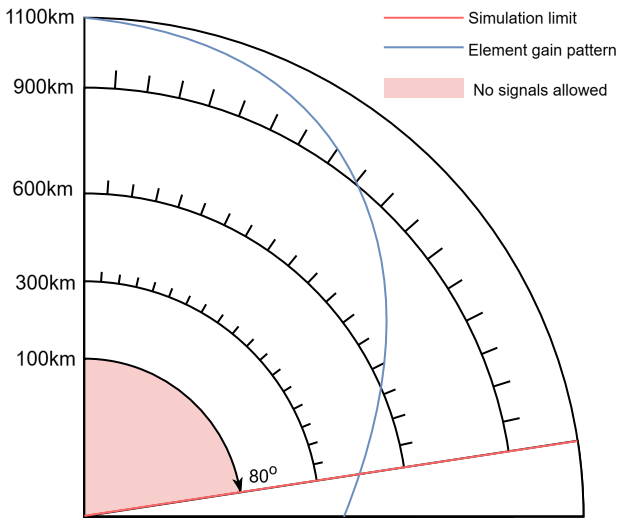

Figure 3.2: The simulation space for simulating the algorithms (Not to scale). A red line at 80° marks the end of the simulation space for SOIs. Circle sectors with notches are where SOIs were placed for DOA estimations. A red area within 100 km marks where no signals were allowed. A blue line shows the antenna element directional gain approximate appearance.

With the final simulation space for the DOAs described as Figure 3.2, the resulting data from one simulated environment consisted of the measured samples from each antenna element for each single random environment. After this, the SOI was added to the environment data for each DOA that should be simulated. The DOA estimation algorithms were then applied.

3.4.1 General simulations

The analog and digital algorithms were applied slightly differently, because, as described in Section 2.6, the signal processing chains look different for the two applications. Common for both applications is that they were performed once for each measurement, for a time window that was perfectly matched to the SOI. The matched time window was used since it was initially assumed that the SOI had a large enough SIR to any interfering signals, so that decoding the SOI was possible. However, whether decoding was possible was tested later. In the same manner, it was also assumed that it was possible to decode the replies, and therefore specify the samples with SOI pulses. This meant that the total number of samples with interfering signals could be kept as low as possible without removing any pulses containing the SOI.

To replicate the analog signal processing chain in Figure 2.9 in the simulations, the discrete array steering directions for each DOA needed to be decided. In reality there are many criteria on how this is decided, and no obvious convention. The discrete steering directions were selected as $\theta_0 \in \{0°, \pm 15°, \pm 30°, \pm 45°, \pm 60°, \pm 75°\}$, whose main lobes cover the entire space in front of the array well. Since there was no obvious way to pair steering directions with SOI DOAs, DOA estimates were performed in all steering directions. The best DOA estimate was then selected, and the steering direction which it came from was then used to determine if it would have been possible to decode the signal. The simulated signal processing chain is illustrated in Figure 3.3.

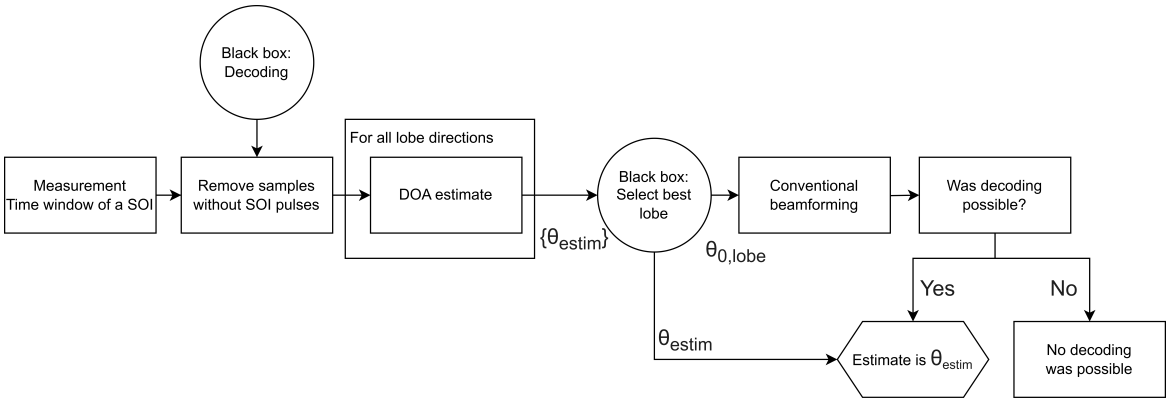

Figure 3.3: Block diagram of how the analog DOA estimation was simulated. For a time window matched to the SOI, the samples with pulses were selected. The DOA was estimated for all lobe steering directions and the best estimate was chosen. It was then determined if the signal could have been decoded. The hexagon is the possible output of the simulation.

Another difference from the signal processing chain in Figure 2.9, is that the simulations simply chose all samples where there was an SOI pulse, instead of selecting the good samples of the pulses which were not as disturbed by any interfering signal. In analogy with why the black box was introduced to decide the lobe direction, whether a sample was classified as good or bad is difficult to define, and was therefore not done at all, which might impact the performance since more of the interfering signals is measured on. Partially though, the function of this black box was instead handled by determining if it was possible to decode the signal.

To determine if it was possible to decode a reply, the SIR was calculated after conventional beamforming in the steering direction was applied. The true SOI's DOA, θ_{SOI}, and all true interfering DOAs θ_m and ranges R_m were then used to select the interfering reply that was causing the worst possible SIR as

$$\text{SIR} = \min_m 20 \log \left(\frac{G_{\theta_0}(\theta_{\text{SOI}})/R_{\text{SOI}}}{G_{\theta_0}(\theta_m)/R_m} \right) \tag{3.6}$$

where $G_{\theta_0}(\theta)$ is the directional gain for the array steered in the direction θ_0 by conventional beamforming as calculated in (2.6). If the SIR $\geq$ 6 dB, the signal was considered possible to decode and the measurement was saved, otherwise it was disregarded. The probability of decoding P_{dec} for each DOA, could then be calculated as the share of replies which could be decoded from all simulations. This parameter also describes how many iterations of the simulation which were disregarded.

For the algorithms utilizing the digital SSR architecture, the processing chain in Figure 2.10 was imitated. Since the aim was to study the potential of these algorithms, some simplifications were made. Decoding the signal was not an objective. Therefore, the simulation never performed any segmentation, estimation of number of signals or preliminary DOA estimations. Instead, the estimation of number of signals was considered as a black box, and consequently, selecting the DOA belonging to the SOI was also considered to be solved by a black box. This resulted in a simulated signal processing chain that is illustrated in Figure 3.4.

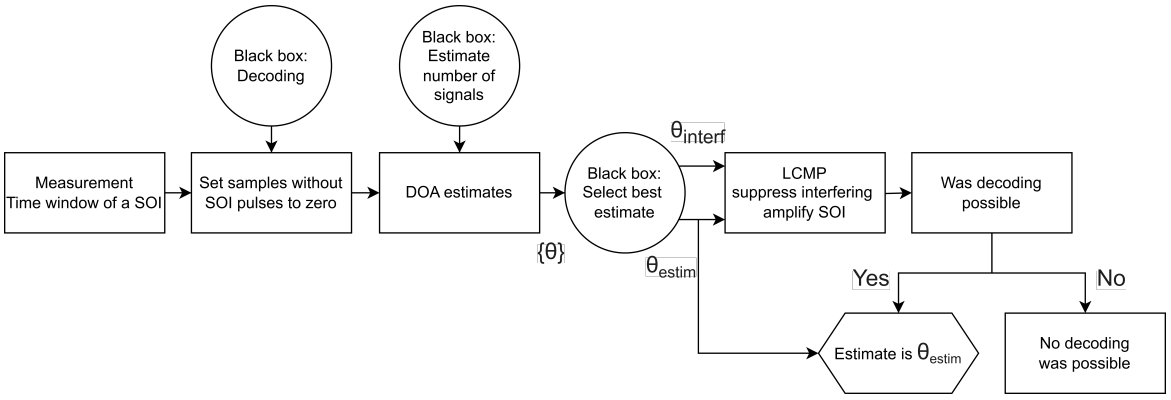

Figure 3.4: Block diagram of how digital DOA estimations was simulated. For a time window matched to the SOI, the samples without SOI pulses were set to zero. DOA estimates were done and the best estimate was selected as an estimate for the SOI DOA. Adaptive beamforming was used to suppress the interfering signals and amplify the SOI before determining if the SOI would have been possible to decode. The hexagon indicates the possible output of the simulation.

Similar to the simulated analog signal processing chain, whether the signal was possible to decode was only checked after the DOA estimate. In the case of the digital simulations, this was done by utilizing the DOA estimates in the adaptive LCMP beamforming explained in Section 2.3.1. Using the estimated DOAs to create a steering matrix $A = \begin{bmatrix} a\left(\hat{\theta}_{\text{SOI}}\right) & a\left(\hat{\theta}_1\right) & \dots & a\left(\hat{\theta}_{M-1}\right) \end{bmatrix}$ with steering vectors, and forming a relevance vector as $g = \begin{bmatrix} 1 & 0 & \dots & 0 \end{bmatrix}$, so that the LCMP algorithm creates weights that amplify the directive gain in $\hat{\theta}_{\text{SOI}}$ and suppresses the gain in $\{\hat{\theta}_m\}$. The weights were calculated as in Equation (2.5). When these weights are applied, the directive gain $G_{\text{LCMP}}(\theta)$ calculated from (2.6) is used to determine the worst possible SIR caused by the interfering signals as

$$\text{SIR} = \min_m 20 \log \left(\frac{G_{\text{LCMP}}(\theta_{\text{SOI}})/R_{\text{SOI}}}{G_{\text{LCMP}}(\theta_m)/R_m} \right). \tag{3.7}$$

As in (3.6), this was also required to be SIR $\geq 6\,\text{dB}$ for a reply to be considered possible to decode.

3.4.2 Fixed interfering signals

To further study the DOA estimation algorithm's behavior in certain situations, another version of the simulation environments was implemented where the number of interfering signals and their DOAs were pre-specified. This made it possible to study how the algorithms behaved in proximity to interfering signals and how much influence an interfering signal actually had on a measurement.

The main difference from the general type of simulations is that the number of interfering signals are fixed with fixed DOAs. Since this makes the symmetry no longer hold, these simulations are also done for all SOI DOAs $\in [-80, 80]^\circ$ with 0.5° spacing. Because the number of randomized parameters for each environment is lower in these types of simulations, these simulations would converge quicker. Hence, these simulations were only run for 50 000 iterations per environment.

4
Results and analysis

This chapter presents the results produced by the method described in the Chapter 3. For each simulation, the error statistics of the DOA estimates are presented as mean bias error and standard deviation which can be used to estimate the accuracy and precision. For all figures, the probability of decoding, P_{dec}, is presented below the error statistics. This is to give context to the error statistics, since accurate estimates of a DOA when P_{dec} is very low are not as useful in a practical implementation as a decent DOA estimate when the signal is more probable to decode. Furthermore, where P_{dec} is low, there is less data from which the bias and standard deviation are calculated.

The results are divided into a Section 4.1 concerning the general simulation described in Section 3.4, and 4.2 concerning the more specific simulations described in 3.4.2. The specific simulations were only performed for the monopulse and ESPRIT algorithms since they were the most prominent algorithms in the general simulations. The analysis is presented along with the figures of the relevant simulations.

As was described in Section 3.2, an environment is characterized by the distance to the SOI source and the intensity of interfering signals in the simulation time window. To reduce the number of plots, improve readability and make it easier to compare the algorithms, the results for each algorithm are presented using plots of cases where the environments have the same occurrence intensity of interfering signals. This means that each plot shows the error statistics for one algorithm, one occurrence intensity of interfering signals, and three distances to the SOI, which can also be considered as SNR levels.

4.1 General simulations

Five different intensities of interfering signals were simulated, 0, 0.0026, 0.0066, 0.013 and 0.026 /km^{2}s. All four DOA estimation algorithms presented in 2.4.2 were used to make DOA estimates in these five cases. There were a total of 100 000 iterations simulated for each environment so the simulations had a chance to converge. In cases where P_{dec} was very low ($\leq 10\%$), there was insufficient data for the simulations to converge. Hence, the algorithms failed to provide reliable estimations in these environments, meaning that there was insufficient data for any meaningful statistical analysis. Because of this, any such data where a simulation clearly had not converged, is not presented. In some cases it might be questionable if the simulation has converged, this is then emphasized. The first case was without interfering signals, so that a baseline could be established and the basic characteristics of the algorithms could be seen. The results of this case are presented in Figures 4.1.

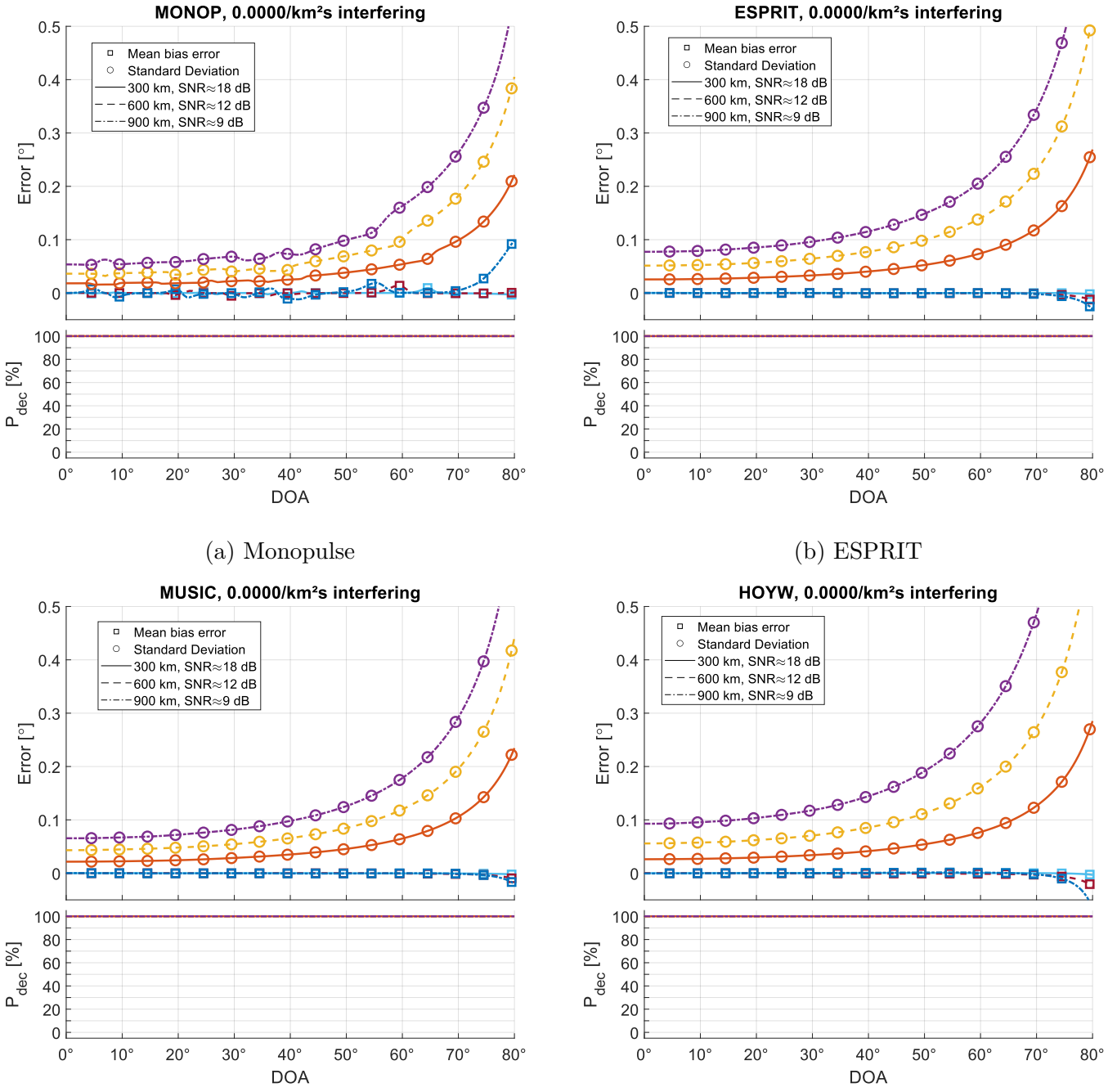

(a) Monopulse

(b) ESPRIT

(c) MUSIC

(d) Higher-order Yule-Walker

Figure 4.1: Algorithm's performance for an intensity of 0.0 interfering signals/km^{2}s. The error statistics for each algorithm are presented above P_{dec}. P_{dec} is constantly 100% for all algorithms since no SIR quota can be made. There are slight bumps in the monopulse bias and standard deviation because of the discrete array steering directions. The standard deviation increases with larger DOAs because of increased sensitivity at higher DOAs as explained in Appendix A.1. The mean bias error of all algorithms deviates at 75°, which caused by smaller antenna size orthogonal to higher DOAs.

In Figures 4.1, P_{dec} is seen to be constant at 100%. This is because it is based on the SIR,

which does not exist when there are no interfering signals. This means that the SOI was always possible to decode in these simulations, since the SNR was assumed to be sufficient for decoding in all cases.

While the mean bias error is close to zero for all algorithms, the monopulse has small sections where it peaks. This can be explained by the discrete array steering directions used for the analog SSR architecture, in which the monopulse is applied. These peaking sections, centered around 7.5°, 22.5°, 37.5° and 57.5° are clearly consistent with the mid points between the antenna array steering directions that are used: $\theta_0 = n \cdot 15°$ where $|n| \leq 5$ is an integer. This bias can be explained by considering the array phase spectrum, where the beamforming can be described as a filtering behavior with some center frequency corresponding to the steering direction, and the bandwidth representing the lobe width in the array phase spectrum. The signal would be a narrow pulse centered around the array phase representing the DOA of the signal. Consequently, measurements on signals with DOAs near the lobe edges are biased toward the lobe's steering direction due to the asymmetrical attenuation of the signal pulse. This bias also contributes to a lower precision near those DOAs, as the estimates at the lobe edges are performed on more attenuated signals, making it sensitive to noise and interference. Since the other algorithms utilize adaptive beamforming, the SOI rarely lies at the edge of any lobe, which is why their mean bias errors are more consistently zero.

By analyzing the standard deviation, it is seen that the precision of all algorithms displays similar characteristics in Figures 4.1. At greater DOAs, the precision decreases, creating a slope in the plot. And for DOAs closer to the antenna normal, the precision is almost consistent. This consistent area could be a consequence of the effective antenna area, which is the antenna size orthogonal to these directions, which becomes smaller further away from the antenna normal. The monopulse in Figure 4.1 (a) most clearly displays this behavior, since its antenna lobes are steered in discrete directions. The other algorithms in Figures 4.1 (b,c,d) display a more gradual transition caused by the individual antenna elements directional gain $\cos^2(\theta/2)$, because they do not rely on discrete array steering directions.

The impact of the SNR on the standard deviation in Figure 4.1 can be described by the difference in standard deviation between the environments with different SNR. Studying this, it is seen that all algorithms perform better at higher SNR, which is expected because it makes the signals easier to distinguish. It is also visible that HOYW has the largest spaces between the different SNR environments, and its precision is therefore the most degraded by the lower SNR.

At the edge of the simulated DOAs, starting around 75°, the bias of the measurements deviate from zero for all algorithms in Figures 4.1. For the monopulse, this is explained by the fact that antenna lobes steered to this angle become very wide, while the simulation space is limited at 90°. With a maximum steering direction of 75°, any measurements beyond this point are performed with a steering direction to the left of the DOA. Remaining algorithms in Figures 4.1 (b,c,d) mainly experience effects of observations from a steep angle, decreasing the effective area of the antenna array in a direction orthogonal to the DOA.

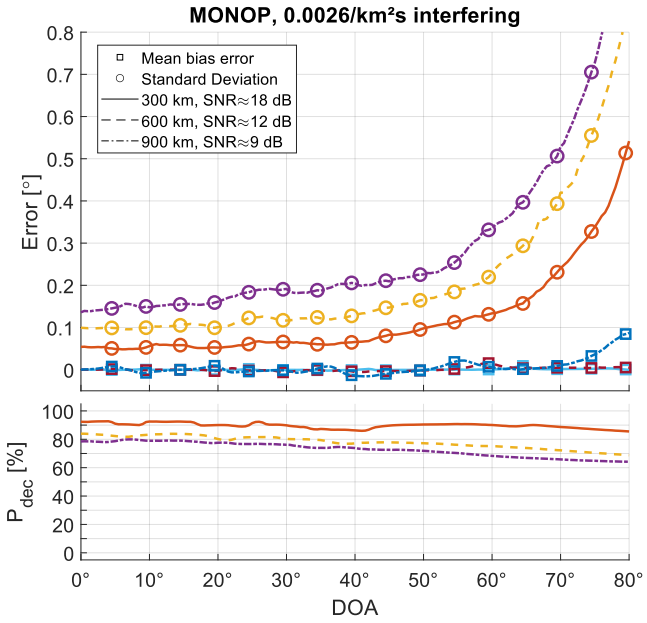

(a) Monopulse

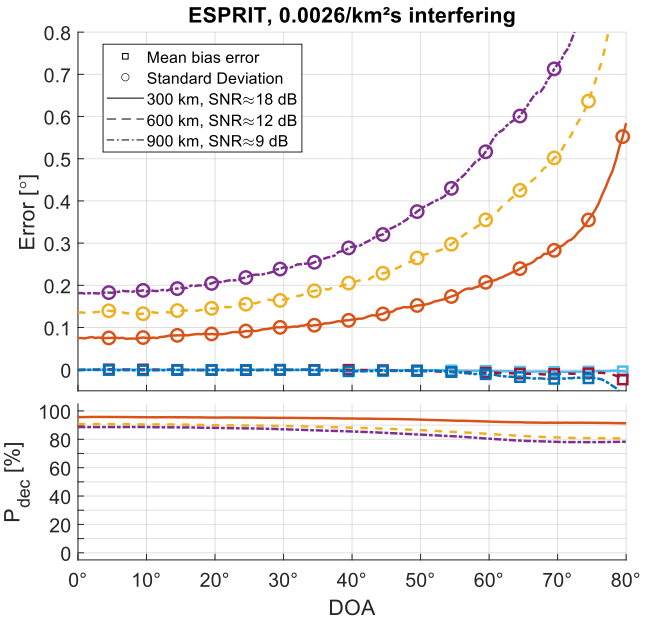

(b) ESPRIT

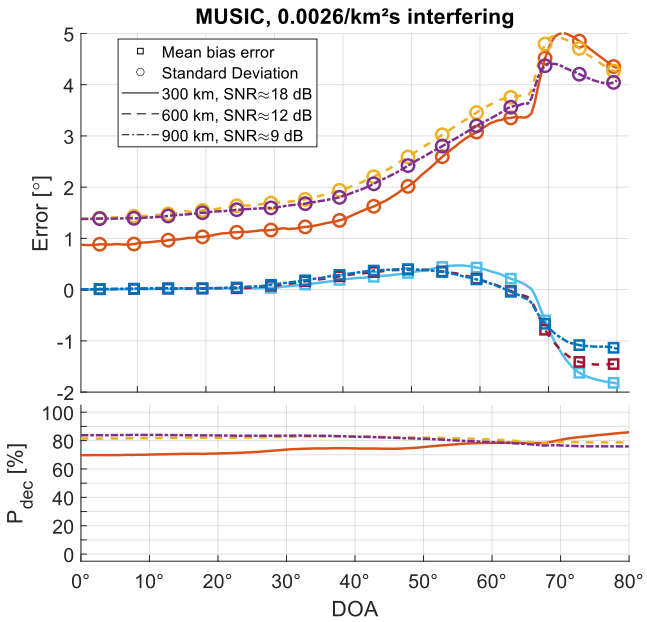

(c) MUSIC

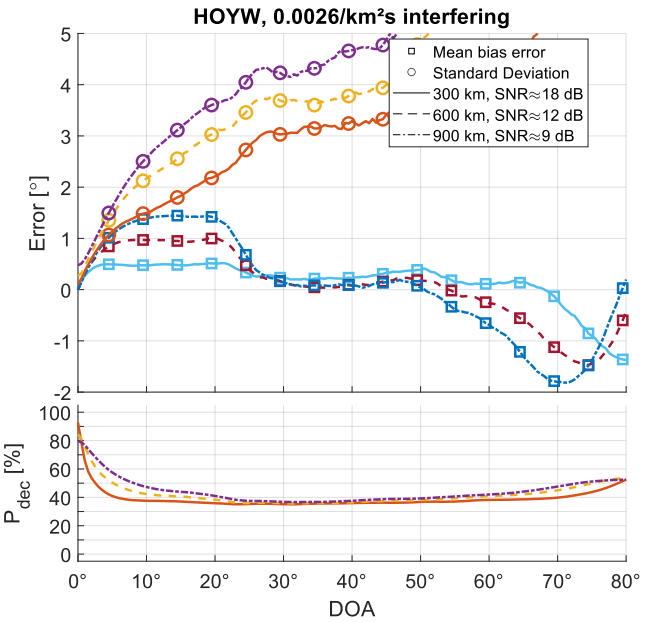

(d) Higher-order Yule-Walker

Figure 4.2: Algorithm's performance for an intensity of 0.0026 interfering signals/km^{2}s. The error statistics for each algorithm are presented above P_{dec}. Note that plot (c) and (d) have different scales on the vertical axis. The presence of interfering signals enables calculations of SIR quotas, yielding scenarios where SOI cannot be decoded, which is represented by P_{dec} plots. HOYW's poor P_{dec} and low precision describe the algorithm's poor performance at the presence of single interfering signals. MUSIC also displays low precision, but its higher P_{dec} indicates better handling of interfering signals compared to HOYW. MUSIC's lower P_{dec} for higher SNR might be caused by the usage of the noise subspace in the algorithm. The high P_{dec} for ESPRIT implies that the algorithm is good at estimating DOAs of all signals, resulting in appropriate beamforming suppressing interfering signals.

When the interfering signals were introduced, it was possible to form SIR quotas as in (3.6) and (3.7). The interfering signals mean that the measurement of the SOI could be disturbed, causing the decoding of the signal to fail and P_{dec} to decrease from 100%. This began to separate the analog and digital architectures, since they used different methods to classify if a signal was possible to decode or not. The strengths of the digital algorithms in the context of the signal processing chain, are that they could utilize digital beamforming. The result of this becomes clear when P_{dec} is studied. Disregarding HOYW and MUSIC which display poor precision, ESPRIT in Figure 4.2 (b) shows better P_{dec} than the monopulse in Figure 4.2 (a), especially for the cases with lower SNR. This can be attributed to the suppression of interfering signals using the LCMP beamforming. To some extent, this also means that the set of simulations from which the error statistics are calculated is larger for the digital algorithms, and this could explain the lower precision.

While all algorithms are somewhat affected by the presence of interfering signals as seen in Figure 4.2, ESPRIT and monopulse are the least affected. Both of their standard deviations were contained below 0.5°. With a close look, it can be seen that the monopulse estimates yielded a lower standard deviation than ESPRIT, but that ESPRIT had a higher, and more consistent P_{dec}. Meanwhile MUSIC and HOYW had standard deviations above 1° for most DOAs. The HOYW algorithm especially, stands out with the lowest precision and by far the lowest P_{dec}. From this it is clear that HOYW fails in the presence of single interfering signals. When even more interfering signals were introduced, the simulations of HOYW failed to converge and produce sufficient data to calculate any meaningful error statistics.

In the MUSIC results, there are some interesting properties. Most notably, P_{dec} was slightly lower for higher SNR, and the standard deviation of the errors was slightly lower for the 9 dB environment than for the 12 dB environment. This is unexpected since it theoretically should be harder to find the signal in a low SNR environment. However, since MUSIC utilizes the noise subspace, the lower amount of relative noise could impact the subspace's precision and suitability for the DOA estimation purpose.

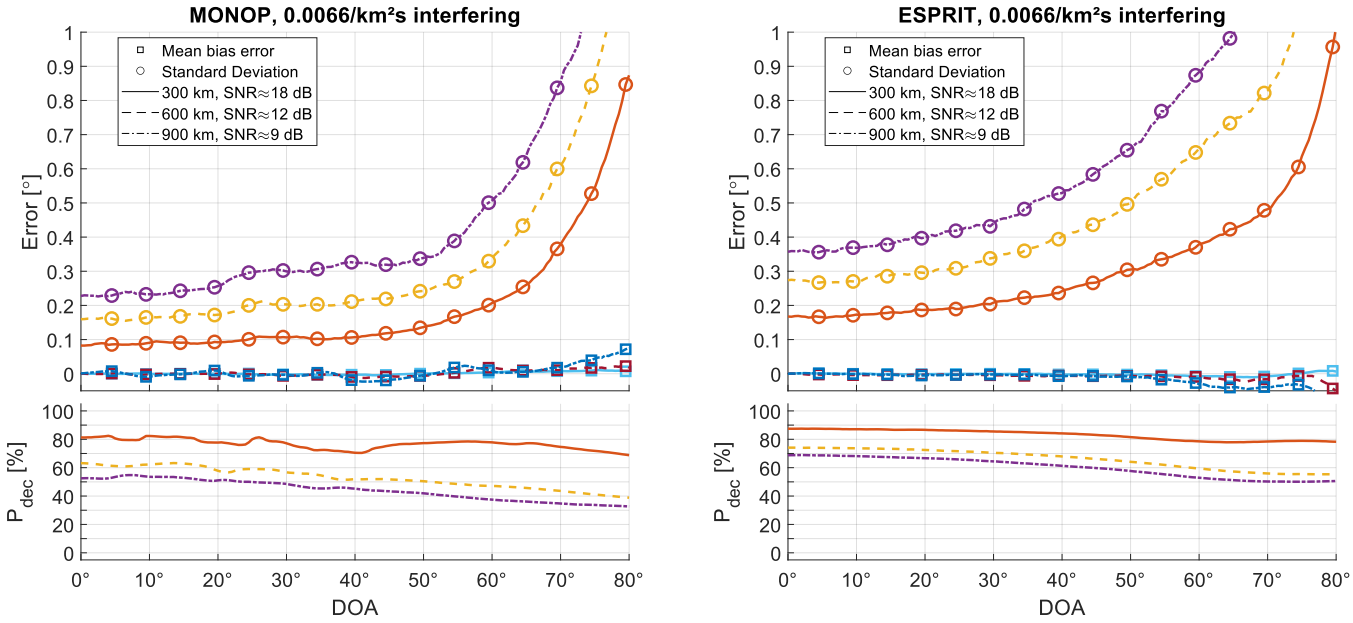

(a) Monopulse

(b) ESPRIT

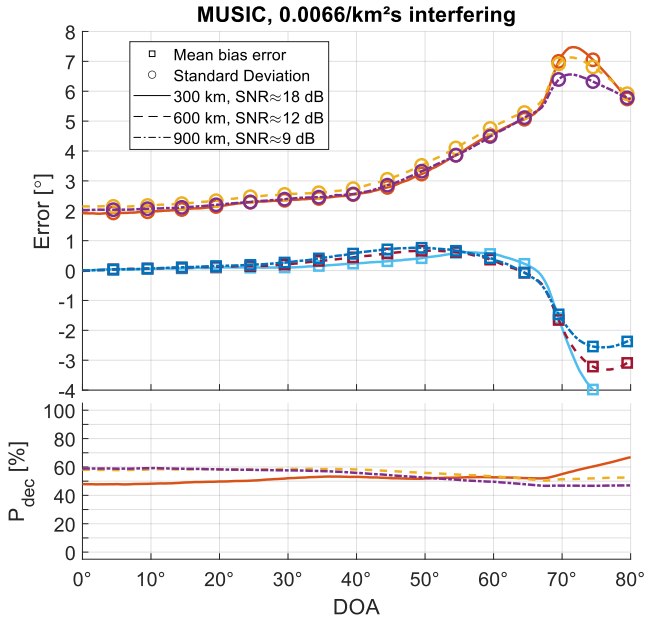

(c) MUSIC

Figure 4.3: Algorithm's performance for an intensity of 0.0066 interfering signals/km^{2}s. The error statistics for each algorithm are presented above P_{dec}. Note that plot (c) has a different scale on the vertical axis. HOYW is not included because of the very poor P_{dec}. ESPRIT displays a greater SNR dependency for DOAs around 60°. P_{dec} is affected for all algorithms compared to the results in Figure 4.2. Monopulse displays a hill in standard deviation centered around 30°, probably caused by discrete array steering directions.

In Figure 4.3 the results for HOYW are not included because as was explained, it displayed a very poor P_{dec}. With this many (and more) interfering signals, the simulation had not con-

verged and therefore gave unreliable results.

In Figure 4.3, the precision of ESPRIT starts to display a greater SNR dependency for SOI DOAs around 60°, where the algorithm performs better in the 18 dB environment than the lower SNR environments. This indicates that the steepness of the slopes in standard deviation is not linearly dependent on SNR since this change in SNR dependency per SOI DOA appears slowly. After about 75°, the standard deviation spikes for all environments, which is natural behavior, as was explained in Appendix A.1.

Notably, the monopulse in Figure 4.3 (a) starts to display further effects of the discrete array steering directions, as the standard deviation has a small but noticeable hill centered around 30°. This hill is an effect of side lobes, which will be visualized and explained more thoroughly with specific examples in Section 4.2 and Figure 4.9. Another effect of the discrete array steering directions is the region with almost constant standard deviation for DOAs closer to the antenna normal in Figure 4.3 (a). For greater DOAs, the standard deviation increases, causing a slope in the plot. These characteristics can be seen for the other algorithms in Figures 4.3 (b,c) as well, where this is instead caused by the decreasing effective antenna size, orthogonal to the DOA.

As P_{dec} in Figures 4.3 decreased for all algorithms relative to Figures 4.2, the difference between the monopulse and ESPRIT in P_{dec} become significant, where ESPRIT generally has around 15 percentage points higher P_{dec} across most SOI DOAs. Since the difference in standard deviation between the two algorithms remains about the same, it can be said that ESPRIT handles the increasing number of interfering signals better than the monopulse so far.

In Table 3.1 it is found that the intensity of 0.013 interfering signals/km^{2}s is where the number of interfering signals drawn from the Poisson distribution is probable to exceed five, meaning that the digital algorithms attempt to estimate five DOAs in a measurement where there are more than five signals. The estimates from the digital algorithms are then a combination of the real DOAs present in a measurement. If the SOI is relatively weak in this case, the estimate might become very influenced and biased towards the other DOAs in single simulations. This mostly contributes to a decrease in P_{dec} for ESPRIT and MUSIC, since the estimated directions used in the adaptive beamforming become worse and may result in amplifying the wrong signal or suppressing the SOI. This explains the decrease in P_{dec} for MUSIC and ESPRIT in Figures 4.4 (b,c) relative to P_{dec} in Figures 4.3 (b,c).

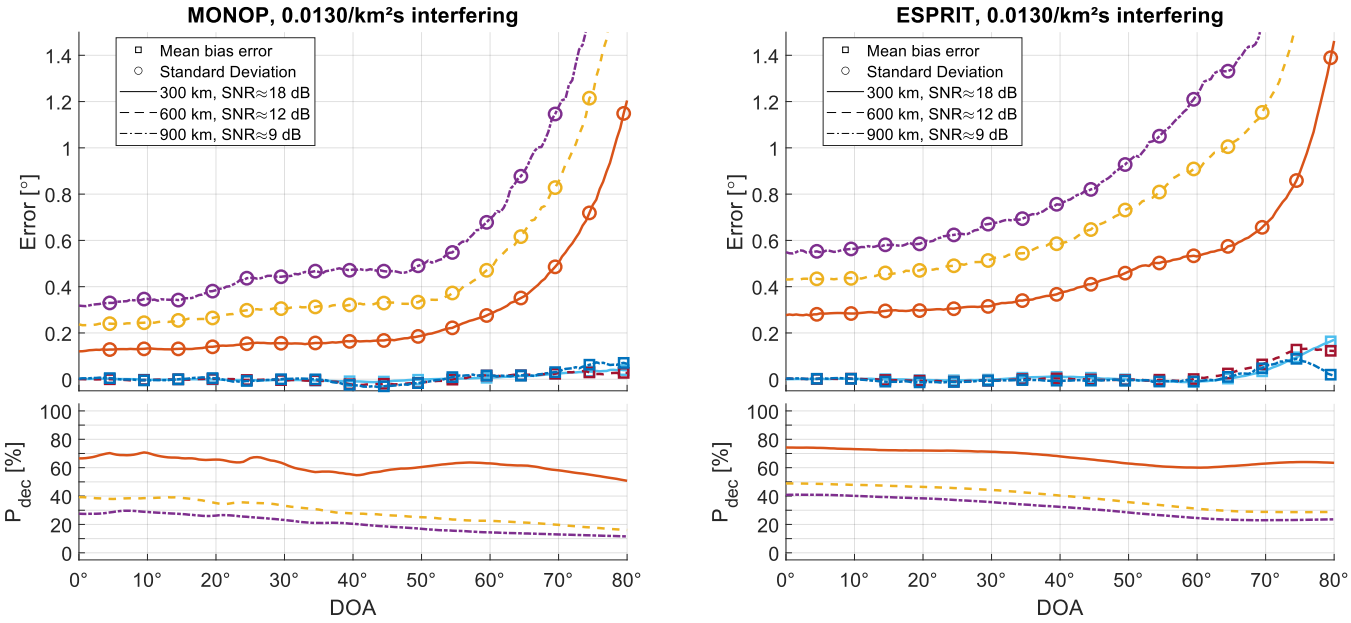

(a) Monopulse

(b) ESPRIT

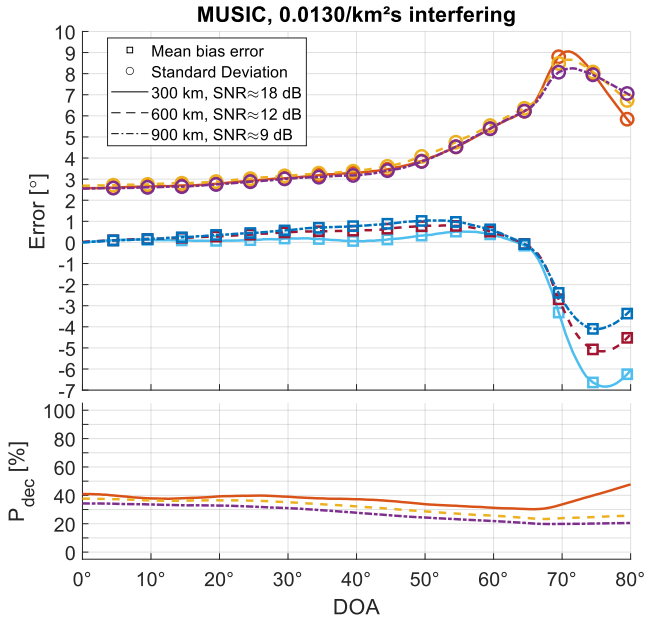

(c) MUSIC

Figure 4.4: Algorithm's performance for an intensity of 0.013 interfering signals/km^{2}s. The error statistics for each algorithm are presented above P_{dec}. Note that the plot (c) has a different scale on the vertical axis. Results for MUSIC show nearly no change from Figure 4.3. Simulations with more than five signals are more common at this interfering intensity. Since ESPRIT and MUSIC are capable of estimating at most five signals, this impacts their P_{dec}.

Rather unexpectedly, the difference in standard deviation for the MUSIC estimates between the different SNR environments in Figure 4.4 (c) has been almost unnoticeable in relation to the values of the standard deviation. Since the standard deviation sums the squares of de-

viations from the mean, the difference between two SNR environments was expected to be greater. This could be a consequence of how the noise subspace is selected, where the number of signals indicates how much of the covariance matrix is selected as the signal subspace leaving the remaining part as the noise subspace. Hence, more DOAs to estimate yield a smaller noise subspace, which could explain the low precision of the estimates.

For the monopulse, it did not matter if there were more than five signals in any other way than that it would increase the probability of interference with the SOI. There is no threshold in the same way there is for the digital algorithms. The number of interfering signals has more of a continuous effect on the monopulse estimates. But with this many, P_{dec} starts to get very low.

For the case with an interfering intensity of 0.026 interfering signals/km^{2}s P_{dec} was very impaired, implying that no simulations converged to reliable results. The results from these simulations are therefore not shown. It is clear that this number of interfering signals made it highly improbable to decode any signal.

4.2 Fixed interfering signals

As was seen in the results from the general simulations, ESPRIT was the most promising digital algorithm based on its higher precision and P_{dec} relative to the other algorithms. To compare it to the benchmarking monopulse algorithm, specific environments with interfering signals whose DOAs were fixed were constructed. Since there are less random variables to consider in this sort of simulation, fewer environments were needed for the simulations to converge. Hence only 50 000 simulations were performed for each of these environments.

To start with, one interfering signal was placed at 36° to study how the algorithms behaved around one single interfering signal.

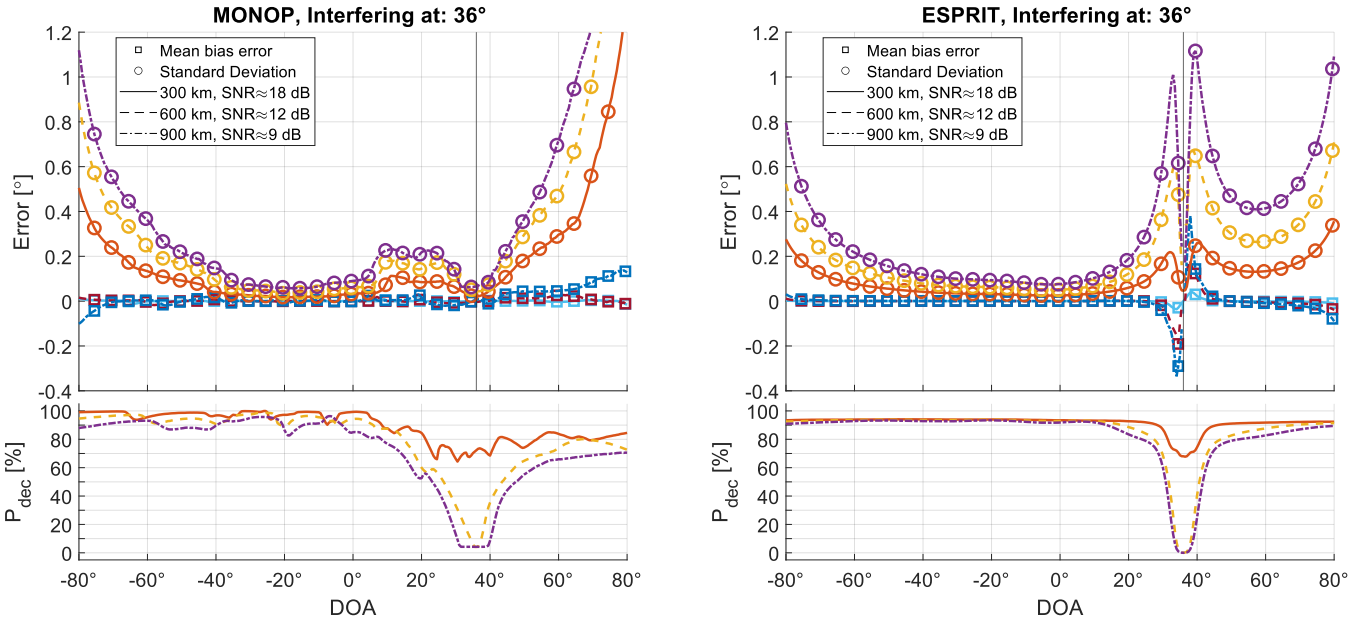

(a) Monopulse

(b) ESPRIT

Figure 4.5: Algorithm's performance when one interfering signal has a fixed DOA at 36°. This is marked with a vertical black line in the plot. The error statistics for each algorithm are presented above P_{dec}. Monopulse shows effects of discrete array steering directions with sections of higher or lower standard deviation and P_{dec}. In array steering direction covering DOAs $[-35°, 0°]$, the interfering signal at 36° lies in a null of directive gain from conventional beamforming. ESPRIT's capability to account for interfering signals is seen by the way its precision is mainly affected around the interfering signal, but generally unaffected for DOAs far away from it.

In Figures 4.5, the interfering signal at 36° clearly affects the algorithms. Most clearly in the precision and P_{dec} which deviate from the smooth results in Figure 4.1 where no interfering signals were present. Perhaps counterintuitive at first, the errors seem to decrease in close proximity to the interfering signal. But by considering how the interfering signal causes a bias in the direction of the interfering signal's DOA, it is easily understood that if the two signals come from the same direction, the bias introduced by the interfering signal alight with the true DOA. This also explains why the bias for ESPRIT in Figure 4.5 (b) goes both in the negative and positive directions, depending on which side of the interfering signals the SOI lies.

Comparing the precision and P_{dec} of the monopulse and ESPRIT in Figure 4.5 (a) and (b), the strength of ESPRIT is displayed. Where the monopulse is affected by the interfering signal over a large span of DOAs, ESPRIT has a clear limit where the interfering signal has influence on the measurement. This is because for the monopulse, all measurements where the array steering directions yield directional gain which amplifies the interfering signals, will be disturbed. And because of the side lobes in both sum and delta channels caused by conventional beamforming, it even affects the measurements at DOAs which are far away from the interfering signal's DOA. This can clearly be seen by the fact that P_{dec} is affected at almost all DOAs in the monopulse estimates.

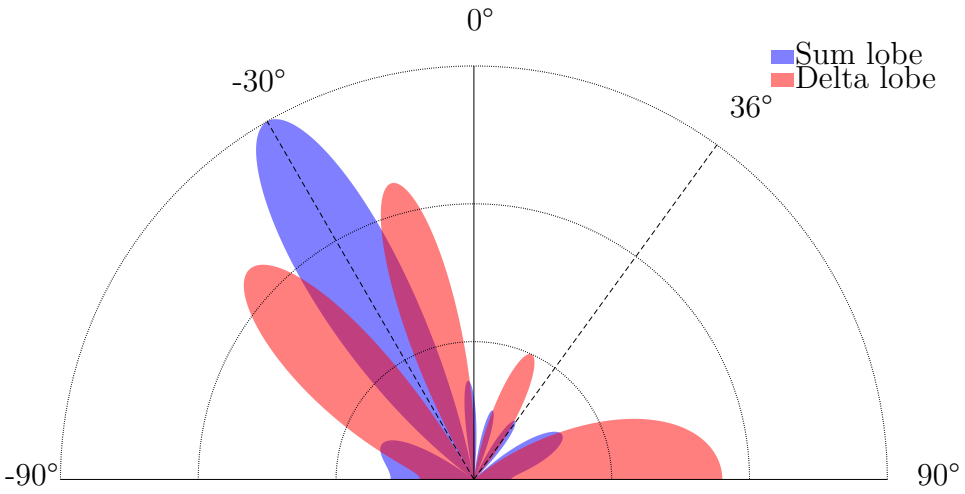

Figure 4.6: Directional gain of sum and delta channels for an antenna array steered in $\theta_0 = -30°$ by conventional beamforming. An interfering signal marked at 36° inside a gain null.

The effects of side lobes can also be seen in the standard deviation of Figure 4.5 (a) for DOAs $\in [-35°, 0°]$, where there is a valley in the standard deviation. At this point the interfering signal at 36° instead avoids any sidelobe with larger gains as is seen in Figure 4.6. When the antenna array was steered in a direction $\theta_0 = -30°$ by conventional beamforming, it is observed that the interfering signal at 36° ends up in a null of the directive gain. This explains why the standard deviation in Figure 4.5 (a) has a valley where the lobe is steered in $\theta_0 = -30°$, and why the main lobe would cover an SOI which lies there. Beyond about −35°, the SOI ended up outside this lobe, and therefore other antenna array steering directions were chosen. With the lobes steered in other directions, the interfering signal at 36° did not end up in a null of the directive gain, resulting in more distorted estimates.

Meanwhile, in Figure 4.5 (b), ESPRIT has a rather narrow area where the interfering signal disturbs the measurement. Outside of this area, at e.g. 60°, ESPRIT was capable of estimating both DOAs accurately, yielding a standard deviation of around 0.18° to 0.4° and $P_{\text{dec}} \geq 80\%$. Meanwhile, the monopulse in Figure 4.5 (a) had a standard deviation around 0.3° to 0.7° and a significantly lower $P_{\text{dec}} \in [65, 85]\%$. This is because the analog architecture could not account for the interfering signal as the digital architecture could. The digital architecture applied adaptive beamforming to suppress the interfering signal which increased P_{dec}.

With this plot, it can also be explained why ESPRIT's error statistics generally displayed higher standard deviation than the monopulse. Since the standard deviation weights deviations from the mean quadratically, and the errors in proximity of an interfering signal becomes larger for ESPRIT, its standard deviation is formed rather by the errors in proximity of interfering signals than by DOAs far away from them. The adaptive beamforming used by the digital architecture also meant that it was possible to decode more difficult cases. This means that the statistics for ESPRIT were calculated on more challenging data, whereas the most challenging cases were discarded when calculating the monopulse statistics. If the statistics would have been calculated only from results where both SSR architectures were able to decode the signal,

ESPRIT's precision would be much better.

Another notable property of these plots is the depth of the valleys of P_{dec}. Since an SOI from the interfering DOA would only be classified as possible to decode if the SIR was $\geq 6\,\text{dB}$ the SIR equations (3.6) and (3.7) become

$$\text{SIR}|_{\text{dB}} = 20 \log \frac{R_{\text{interf}}}{R_{\text{SOI}}}. \tag{4.1}$$

In the case where the SOI is placed 600 km from the array, and the interfering signals are not placed further away than the horizon at 1100 km from the array, the SIR was 5.3 dB. If the SOI was placed at 900 km, it was impossible to reach the 6 dB SIR required to decode the signal.

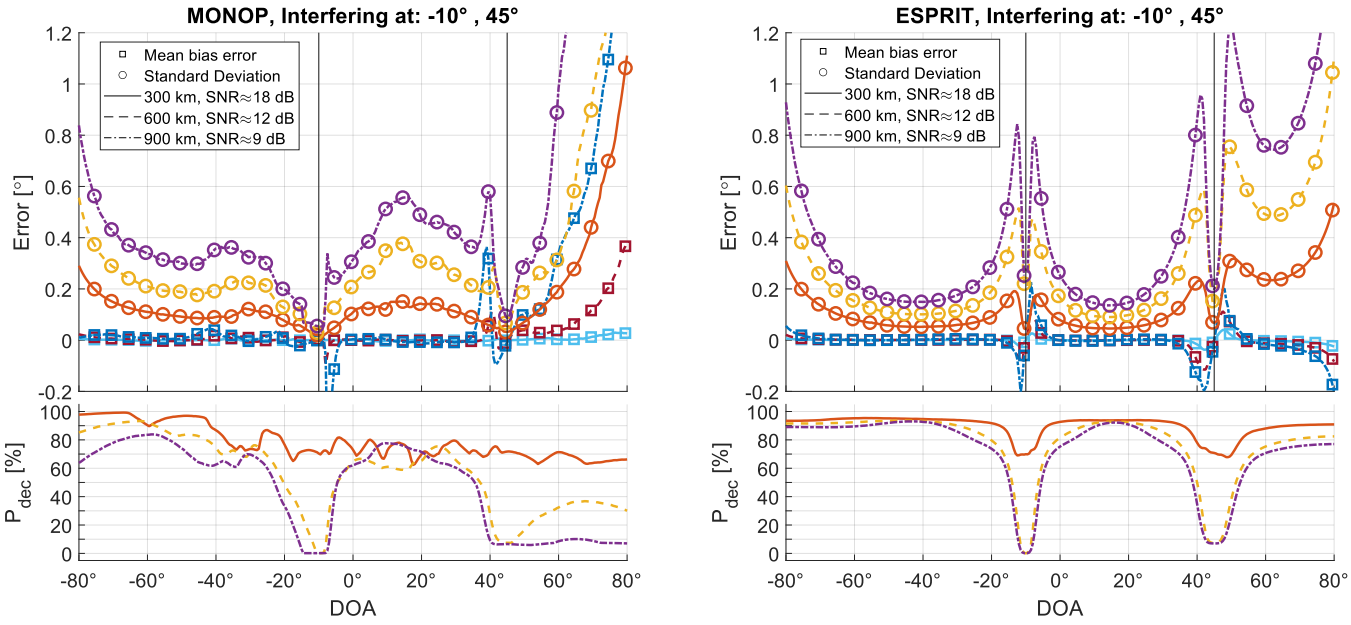

(a) Monopulse

(b) ESPRIT

Figure 4.7: Algorithm's performance when two interfering signals have fixed DOAs at $-10°$ and $45°$. These are marked with vertical black lines in the plot. The error statistics for each algorithm are presented above P_{dec}. ESPRIT still manages to account for the interfering signals, yielding results that are not as affected by them far away from the interfering signals. The monopulse has problems where the interfering signals appear in most main or side lobes, disturbing the estimates. For monopulse estimates above $40°$ the lobe is very disturbed, causing lower SNR environment simulations to yield extremely poor P_{dec}.

By placing two interfering signals at $-10°$ and $45°$ respectively, it is possible to study if and how multiple interfering signals might cause a greater disturbance to the measurements together.

In Figure 4.7 it is seen that the algorithms are affected in two different ways. The monopulse clearly experiences problems with side lobes as in Figure 4.5 (a) and entire disturbed lobes as combinations of the two interfering signals. While ESPRIT is capable of taking the interfering signals into consideration, to estimate them as independent problems. This means that as long

as the interfering signals are separated so that they are outside of each other's areas of influence, both of the interfering signals are accounted for when estimating the SOI DOA. This explains why the standard deviation at some distance from the interfering signal's DOAs was rather low for ESPRIT, but still disturbed for monopulse.

For DOAs above 40° in Figure 4.7, P_{dec} is seen to drastically decrease for the two lower SNR environments. The 18 dB environment also has an impaired P_{dec} across almost all DOAs. This is also an effect of side lobes. There are few array steering directions where interfering signals will not occur in either side or main lobes. Above 40° especially, there are no lobes without any interfering signals, which yields very poor P_{dec}.

In this case the space between the two signals made it possible for ESPRIT to separate them well. But if there are two interfering signals close to each other, for example at 40° and 47°, this introduces a problem of determining several DOAs that are close to each other.

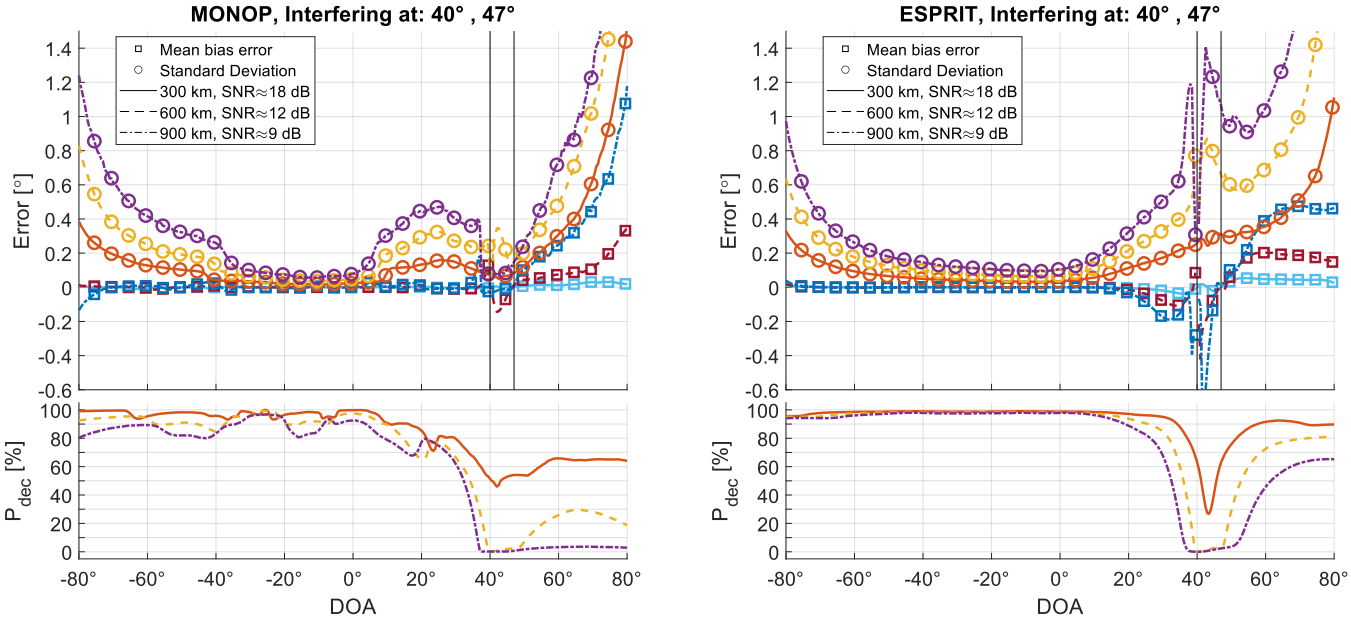

(a) Monopulse

(b) ESPRIT

Figure 4.8: Algorithm's performance when two interfering signals have fixed DOAs at 40° and 47°. These are marked with vertical black lines in the plot. The error statistics for each algorithm are presented above P_{dec}. ESPRIT is capable of compensating for both interfering signals, so that estimates far away from them are seemingly unaffected. The monopulse still experiences difficulties with interfering signals in side lobes. Lobes covering DOAs greater than 40° are still very disturbed.

In Figure 4.8 (b), it is clear that for ESPRIT, the area of influence around the interfering signals increases relative to its size in Figure 4.5. This was expected since the interfering signals were in proximity to each other. The standard deviation of the estimates were also greater in between the interfering signals. This is also expected since, depending on the distances to the two interfering signals, the estimate will be more or less biased towards one of them. Thus,

with many individual cases, the standard deviation increases.

For the monopulse in Figure 4.8 (a), the standard deviation is seen to have a low valley around 0° to −30°. This is yet another example of how steering the antenna array in directions far away from the antenna normal results in side lobes. In this case, the steering directions covering DOAs in the valley has side lobes where there are no interfering signals, similar to the case in Figure 4.6.

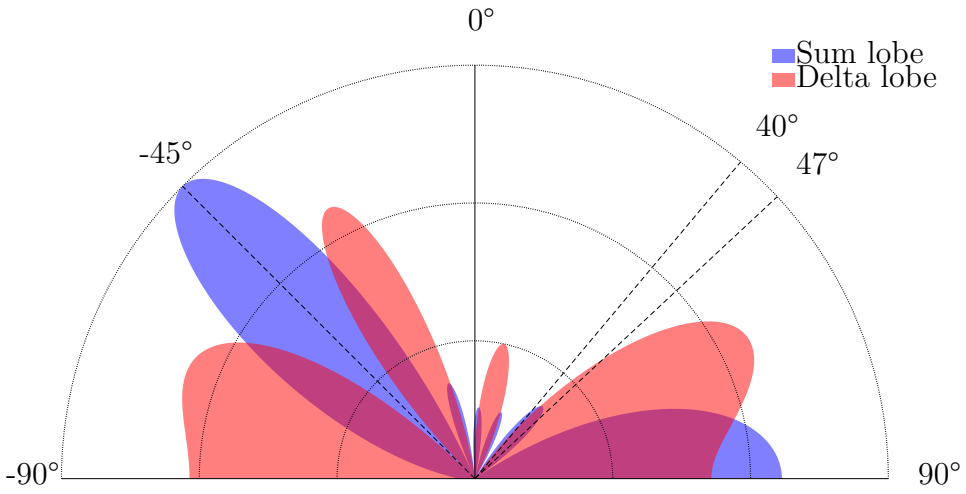

Figure 4.9: Directional gain of sum and delta channels for an antenna array steered in $\theta_0 = -45°$. Interfering signals are marked at 40° and 47° inside a sum side lobe. An interfering signal marked at 47° also inside delta side lobe.

The steering direction $\theta_0 = -45°$ covering DOAs $< -30°$, however, has sidelobes with reasonable gain in both sum and delta channels which pick up both interfering signals and causing disturbances in the measurements. Hence, in Figure 4.8 (a), the lobes steered to positive directions are disturbed by the interfering signals in the main lobes, while the lobes steered at −45° are disturbed by the interfering signals in a side lobe. The lobes covering −30° to 0° are not disturbed by the interfering signals at all.

The same characteristics seen in Figure 4.7 (a) where sidelobes caused very poor P_{dec} for DOAs above 40° can be observed in Figure 4.8 (a). In Figure 4.8 (a) the two interfering signals at 40° and 47° are seen to disturb the measurement in the antenna steering directions responsible for estimates at DOAs $< -40°$. This makes P_{dec} even worse for the monopulse in Figure 4.8 (a).

5
Discussion

A number of interesting characteristics were found in Chapter 4. In this chapter, a comparison of the analog and digital SSR architecture is made, with an emphasis on the characteristics that were found. The comparison is made in the context of how each architecture might affect a practical SSR application. Since no full model of the digital SSR architecture was implemented in this thesis, some possible further studies on subjects relating to the findings in this thesis are also discussed.

5.1 Comparison of SSR architectures

From the results in Chapter 4, it is clearly seen that the most prominent digital algorithm is ESPRIT. Apart from providing the most precise estimates of the digital algorithms, it also yielded the highest probability of decoding, P_{dec}. For a practical implementation, ESPRIT could therefore be considered the best candidate of the digital algorithms.

Given this, an application of the entire digital signal processing chain described in Section 2.6 has not been studied. While it might be a bold assumption that all parts of the flow chart in Figure 2.10 describing the process could be solved perfectly, it makes it easier to comprehend the difference from the analog architecture. Thus, the basic concept, which in some sense was implemented in the simulations as described by the flow chart in Figure 3.4 is considered as practically possible. This concept allows a number $M < N$ signals arriving to the array with N elements, to be treated separately by adaptive beamforming and DOA estimations through ESPRIT.

When comparing the digital signal processing chain to the analog one shown in Figure 2.9, a key difference is the impact of the array steering direction. When the entire processing is done one direction at a time, it prevents reception of replies from any other directions. This limits the coverage of the interrogator at any one moment in time. In a case where replies are only triggered by interrogations from the same interrogator, this limitation is acceptable. However, if there is interest in decoding and measuring replies not prompted by the original interrogator, this constraint becomes an obstacle.

Although an interrogator's primary function is to process the replies it triggers, there are benefits to processing additional replies as well. One reason for this is that not all replies are triggered by interrogations. For example, ADS-B squitter is a Mode S reply which is spontaneously transmitted by transponders without being triggered by an interrogation [14, p. 5-12]. To create a complete situational image of an airspace for an ATC unit, information about all

aircraft present in an airspace is relevant. A digital architecture, capable of providing more extensive simultaneous coverage is therefore advantageous.

A significant advantage of the digital SSR architecture with ESPRIT was the increased P_{dec}. In the general simulations presented in Section 4.1, across nearly the entire range of SOI DOAs, the digital architecture consistently had a P_{dec} at around 15 percentage points higher compared to the analog architecture. In simulations with fixed interfering DOAs, the main distinction between the architectures was in how the interfering signals affected precision and P_{dec} across the range of DOAs. The digital architecture experienced more local impacts, with a valley in P_{dec} around the interfering signal's DOA. Meanwhile, the analog architecture was affected across the entire range of SOI DOAs even if it was less affected compared to the digital architecture in close proximity to the interfering signal.

So far, the digital SSR architecture, not being limited to processing specific antenna lobes one at a time, and decoding more replies, advocate the use of a digital architecture. But another important aspect in the SSR perspective is accuracy of the DOA measurements. In this category, the analog architecture seemingly displayed a better performance in the general simulations from Section 4.1. One possible explanation for this, is that it only considers one antenna steering direction at a time. Therefore it is probable to avoid interfering signals in the scenarios with sufficient SIR. This makes its estimates very precise, with standard deviations at an order of a few 0.1°. Though ESPRIT's performance was still highly precise, with errors in the same order of magnitude as the monopulse, the difference was less than a factor of two in relevant DOA ranges.

To bear in mind with this result, is that the higher P_{dec} of ESPRIT meant that the error statistics calculated from ESPRIT's results were calculated on a data set which included cases where the analog architecture was unable to decode the signal. In these cases, the SOI was more disturbed by interfering signals, which probably yielded worse estimates for both hardware architectures. The fact that these cases were included in the error statistics for ESPRIT, but not for the monopulse, gave the monopulse an unfair advantage, because it disregarded some of the more difficult cases. If the error statistics had been calculated only from cases where both hardware architectures could decode the SOI, ESPRIT's precision would increase [5], while the precision for the monopulse would remain roughly unchanged.

Another property of the SSR architectures is how robust they are against interfering signals. Because the frequencies used for SSR are heavily trafficked, this property becomes an important factor to consider. This property is heavily impacted by the number of antenna elements. More elements mean more narrow lobes, which reduces the probability of interfering signals being present in the lobes. For the digital architecture, this property also limits the number of DOAs which can be estimated in each measurement. By estimating the DOA of more signals, the decoding of an SOI can be improved by taking these interfering signals into consideration. But despite this very discrete limit at five DOA estimates per measurement with the assumed antenna array, the digital and analog architectures were affected similarly when the number of DOAs to estimate exceeded this limit. Though P_{dec} still decreased for both architectures, they both displayed a moderate robustness against interfering signals. In the simulations with fixed interfering signals though, ESPRIT displayed a better robustness against interfering signals, as

it could isolate their impacts to DOAs close to the interfering signals.

To summarize the difference in performance regarding the discussed properties, the digital architecture's performance is roughly described in comparison to the performance of the analog structure in Table 5.1.

Table 5.1: Table describing differences in estimate precision and accuracy, P_{dec}, simultaneous coverage, interference robustness and SNR robustness of the digital SSR architecture in relation to the analog architecture. Note that the classification of the performance is somewhat arbitrary and only done for scenarios where the architectures could decode the signal.

Property	Performance of digital SSR architecture relative to an analog architecture
DOA estimate precision	Worse (Comparing decodable cases)
DOA estimate accuracy	Same
Probability of decoding	Much better
Simultaneously coverage	Much wider
Interference robustness	General simulations: Same Fixed simulations: Better
SNR robustness	Same

The digital architecture's primary weakness in the simulations is the worse precision of DOA estimates. But being aware of this, the advantage of high simultaneous coverage can be leveraged to improve this precision. Specifically, measuring an additional reply from the target is a possibility since it is very improbable that it would escape from the coverage. With a second measurement and DOA estimate, a mean could be formed to improve the precision. This could of course be done with the analog architecture as well, but not without compromising time that could be spent covering another array steering direction.

5.2 Impacts of assumptions

A number of assumptions were made in the implementation of the simulations described in Chapter 3. Some of these were done to impose limitations for this thesis, and some were done to imitate realistic properties. While all assumptions were realistic, they still impact the result in ways that could be unique to the specific assumptions. To understand some of the characteristics that were found and how they might appear differently in other implementations, these are discussed.

A prime example of such an assumption is the antenna array model. There are a number of different parameters for the antenna array which affect its properties. In the context of SSR DOA measurements, the number of antenna elements N is important. Because when using digital DOA estimation algorithms, it sets a limit on the number of replies whose DOAs can be estimated from a given measurement. But any parameter which affects the directional gain

impact the measurements. A wider antenna element spacing, for instance, could theoretically make the antenna beams more narrow and increase the number of sidelobes. Such changes would impact the areas of influence seen around interfering signals in e.g. Figure 4.5 (b) or the sidelobe effects seen in Figure 4.8.

Within the antenna array, the directional gain pattern assumed for the individual elements also affected the results. While the $\cos^2 \theta/2$ pattern is realistic for the directional gain, different antenna designs could provide different patterns. In most of the results, the assumed pattern probably contributed to making the standard deviation of the measurement errors larger for larger DOAs further away from the antenna normal, since the directional gain was reduced at larger DOAs. For any other directional gain pattern, one could expect this standard deviation of the estimates to be lower in directions with higher directional gain.

Another assumption which yielded clear effects in the results is the directions that the conventional beamforming of the antenna array was steered into: $\theta_0 = \{0°, \pm 15°, \pm 30°, \pm 45°, \pm 60°, \pm 75°\}$. As was discovered in the results from Section 4.2, the array steering directions affected the performance of the monopulse algorithm. The positions of the side lobes were found to affect the accuracy and precision as well as the P_{dec}, even when the SOI was spatially separated from any interfering signals. While side lobes are difficult to avoid in antenna designs, their positions are somewhat possible to control. It is therefore probable that other side lobe positions, caused by different antenna designs, would have yielded different results.

In addition to the antenna design, assumptions were also made regarding the signal processing. For instance, it was assumed that the samples without any SOI pulses could be set to zero or removed. This is one of many ways of dealing with disturbed samples. Other approaches could impact the interference robustness differently for the different architectures. Utilizing the strengths of each architecture to carefully select the method for dealing with disturbed samples, should improve their performance.

An assumption made only for the analog architecture, is that the best array steering directions to estimate each true SOI DOA was used at all times. This is probably not true in most cases. One reason for this is that the array steering directions need to be set before an estimate is performed. Meaning that information about where there are interfering signals has to be available to select the best direction. This becomes a paradox. In practice, the given array steering direction is used for a measurement regardless of whether the direction is suitable. An attempt to make an estimate and decode the message is then performed, which would probably fail unless the direction was suitable. This crucial difference between the assumption and reality implies that the results seen from a real measurement should be somewhat worse than the results in the simulations.

5.3 Continued work

While this thesis covers how some DOA algorithms might perform for an SSR application, many aspects of a digital SSR architecture were assumed. This leaves room for additional studies on subjects that were not covered in this thesis, but could provide additional understanding on how the performance of the DOA estimations is affected.

The signal processing chain in Figure 2.10 was only mimicked in this thesis. An analysis of a complete implementation of this should reveal if it is plausible and if there are alterations which could improve the performance. On the subject of plausibility, studies on how computationally demanding the algorithms and signal processing chains are would provide valuable context in terms of practical limitations.

Since a fixed antenna array model was used for all simulations in this thesis, assumptions on how the antenna properties could affect the results were never tested. Specifically, the number of antenna elements in the array impacts the digital algorithm's performance. This property could therefore have a significant impact on performance at some scenarios. Examining how the antenna model in general affects the performance is therefore a possible topic to further improve performance.

The effects of hardware imperfections was planned as a possible topic in this thesis, there was however insufficient time for this. Incorporating hardware imperfections in the antenna model would make the signal model more realistic. A general analysis of how DOA estimations are affected is done in [15], but only for limited number of interfering signals and cases. To further study and characterize the effects with the goal of compensating for them, a more complex signal model should be used. The hardware effects could then be described as a matrix $\Pi = L\Omega C$, where $L = \text{diag}(l_1...l_N)$ represents the individual amplitudes which the channels of each antenna elements are multiplied with, $\Omega = \text{diag}(e^{i\omega_1}...e^{i\omega_N})$ are the phases applied to signals in each channel, and C is the coupling matrix. In the signal model in (3.4) this would replace A' with $\tilde{A}' = \Pi A'$. This approach makes it possible to investigate how changes to the algorithms could be imposed to compensate for the hardware imperfections as well.

To study the limit of how well it is possible to estimate the DOAs of signals, the Cramér-Rao bound could be studied. The Cramér-Rao bound is a way to determine the highest possible precision to achieve in an estimation problem. Though studies of this limit for DOA estimation problems exist [16], the aspects of an SSR system could impact these results. Knowledge of this limit could reveal how valuable any attempt to improve the performance of the estimation algorithms might be, since an algorithm which is very close to this limit would not be possible to improve much.

Though there are many different SSR modes used in both civilian and military applications, only Mode S long replies were tested in this thesis. The different modes have replies that are structured differently, which may affect the DOA estimation performance. Studies into how the length and modulation of the messages affect the results could therefore be relevant.

6
Conclusion

This thesis has studied the performance of Direction Of Arrival (DOA) estimations performed by a Secondary Surveillance Radar (SSR) on a received reply on Mode S long format. As a reference, an analog architecture was used, where sum and delta channels are formed, creating two digital channels that interact with an antenna array, which was then compared to a digital architecture, where each of the antenna array elements were digitized separate from each other. The analog architecture utilized the monopulse algorithm for estimating DOAs and was set as a benchmark to compare a few different digital DOA estimation algorithms.

While there are many DOA estimations algorithms for a digital SSR architecture, a few of these were tested. Out of the digital algorithms that were implemented, the ESPRIT algorithm was the most prominent. Its estimates were very precise compared to the other digital algorithms, and with low bias, despite the presence of interfering signals. Its implementation in a digital architecture also yielded a higher probability of being able to decode the signal when the adaptive LCMP beamforming algorithm was applied. Far behind ESPRIT's performance comes the MUSIC algorithm, which could still produce estimates in the presence of interfering signals, but with much lower precision. With even worse performance, the Higher-Order Yule-Walker (HOYW) algorithm was heavily affected by the presence of single interfering signals, something which heavily impaired its probability to decode replies.

A main benefit of the digital architecture was the increased probability of decoding, P_{dec}, which is an important metric for an SSR. Whilst studied further in the context of beamforming for an SSR in a thesis preceding this [5], the probability of decoding gives crucial context to the analysis of the results.

Comparing an analog architecture which uses the phase monopulse calculation to a digital architecture with ESPRIT, it comes down to the implementation. While the monopulse was capable of providing more precise measurements than ESPRIT in the cases where it could decode the signal, the analog architecture can only do so one array steering direction at a time, limiting the area it could simultaneously cover. Meanwhile, ESPRIT was capable of simultaneously covering the entire area in front of the array. This implies that it is theoretically possible to make multiple measurements of a target, as long as it transmits more replies. Multiple estimates of the same target's DOA can improve the precision of the DOA estimate of the target.

Together with the results of this thesis, it is important to note that some assumptions and simplifications were made. These regard both antenna design as well as signal processing operations which were assumed to be possible. In whole, the tested digital signal processing chain would need to be studied further in order to determine its plausibility and potential. Though

the potential in terms of DOA estimations was studied in this thesis, a deeper understanding of the strengths and weaknesses of the signal processing chain could improve DOA estimation performance. With additional studies it could also be possible to design different signal processing chains with better performances.

Bibliography

[1] G. Marconi, *Improvements in transmitting electrical impulses and signals and in apparatus there-for*, British Patent GB189612039A, Filed 1896-06-02, Published 1897-07-02, 1897.

[2] American Physical Society. "April, 1935: British patent for radar system for air defense granted to robert watson-watt." (Apr. 2006), [Online]. Available: https://www.aps.org/publications/apsnews/200604/history.cfm (visited on 05/26/2025).

[3] A. Toraño Caicoya, M. Pardini, I. Hajnsek, and K. Papathanassiou, "Forest above-ground biomass estimation from vertical reflectivity profiles at l-band," *IEEE Geoscience and Remote Sensing Letters*, vol. 12, no. 12, pp. 2379–2383, 2015. DOI: 10.1109/LGRS.2015.2477858.

[4] "Introduction to active electronically scanned array (AESA) radar," Ausairpower.net. (), [Online]. Available: https://www.ausairpower.net/aesa-intro.html (visited on 05/26/2025).

[5] M. Wiklund, "Digital beamforming for a secondary surveillance radar, Numerical and statistical analysis of the ADS-B reception performance for an ssr system with conventional and adaptive beamforming," M.S. thesis, Chalmers University of Technology, 2024.

[6] ICAO, "Annex 10 to the convention on international civil aviation: Aeronautical telecommunications, volume iv — surveillance and collision avoidance systems," Jul. 2014, Montreal, Canada. ISBN: 978-92-9249-537-4.

[7] P. Kildal, *Foundations of Antenna Engineering: A Unified Approach for Line-of-Sight and Multipath*. Kildal Antenn AB, Apr. 2015, Gothenburg, Sweden. ISBN: 978-91-637-8515-3.

[8] H. L. V. Trees, *Optimum Array Processing, Part IV of Detection, Estimation, and Modulation Theory*. New York: John Wiley & Sons, Inc., 2002, ISBN: 0-471-09390-4.

[9] W. C. Chew. "Lecture 26: Radiation fields, radiation fields or far-field approximation," Purdue University. (2019), [Online]. Available: https://engineering.purdue.edu/wcchew/ece604f19/Lecture%20Notes/Lect26.pdf (visited on 05/26/2025).

[10] "Minimum detectable signal - radartutorial," Radartutorial. (), [Online]. Available: https://www.radartutorial.eu/09.receivers/rx51.en.html (visited on 05/26/2025).

[11] P. Stoica and R. Moses, *Spectral analysis of signals*. Prentice Hall, Upper Sadle Ricer, NJ, 2005, vol. 206, pp. 159–164, 165, 166, 284, 285.

[12] P. Stoiuca and Y. Selén, "Model-order selection, A review of information criterion rules," *IEEE Signal Processing Magazine*, vol. 21, no. 19, Jul. 2004, DOI: 10.1109/MSP.2004.1311138.

[13] *Flightradar24, Flightradar 24: Live flight tracker - real-time flight tracker map*, www.flightradar24.com [online], Accessed on: 2025-04-02.

[14] ICAO, "Aeronautical surveillance manual," 2020, Montreal, Canada. ISBN: SBN 978-92-9265-367-5.

[15] C. Reck, U. Berold, J. Weinzierl, and L. P. Schmidt, "Direction of arrival estimation from a secondary surveillance radar signals in presence of hardware imperfections," in *Proceedings of the 5th European Radar Conference*, Oct. 2008, ISBN: 978-2-87487-009-5.

[16] Y. Liang, W. Liu, Q. Shen, W. Cui, and S. Wu, "A review of closed-form Cramér-Rao bounds for DOA estimation in the presence of gaussian noise under a unified framework," *IEEE Access*, vol. 8, pp. 175 101–175 124, 2020. DOI: 10.1109/ACCESS.2020.3026203.

A

Appendix

A.1 Theoretical error limit

Since the carrier wave center frequency can be shifted slightly within a bandwidth, while the frequency in the equation (2.8) is assumed to be constant at 1090 MHz, which is used as center frequency for Mode S replies, some errors are introduced to the equations. By describing the true frequency as $f = f_0 + f_\Delta$ and solving for θ_{DOA}, how the f_Δ affects the estimates from an optimal estimation can be studied. The maximum theoretical error for each θ_{DOA} can be described by the function

$$\Delta\theta_{\text{DOA}} = \hat{\theta}_{\text{DOA}} - \theta_{\text{DOA}} = \arcsin\left(\frac{f_0 + f_\Delta}{f_0}\sin(\theta_{\text{DOA}})\right) - \theta_{\text{DOA}}. \tag{A.1}$$

In Figure A.1, the maximum error for DOAs in the range $[0°, 90°]$ is displayed for the cases $f_\Delta = 0.5$ MHz, 1 MHz and 2 MHz. The three different values for f_Δ are shown as separate lines.

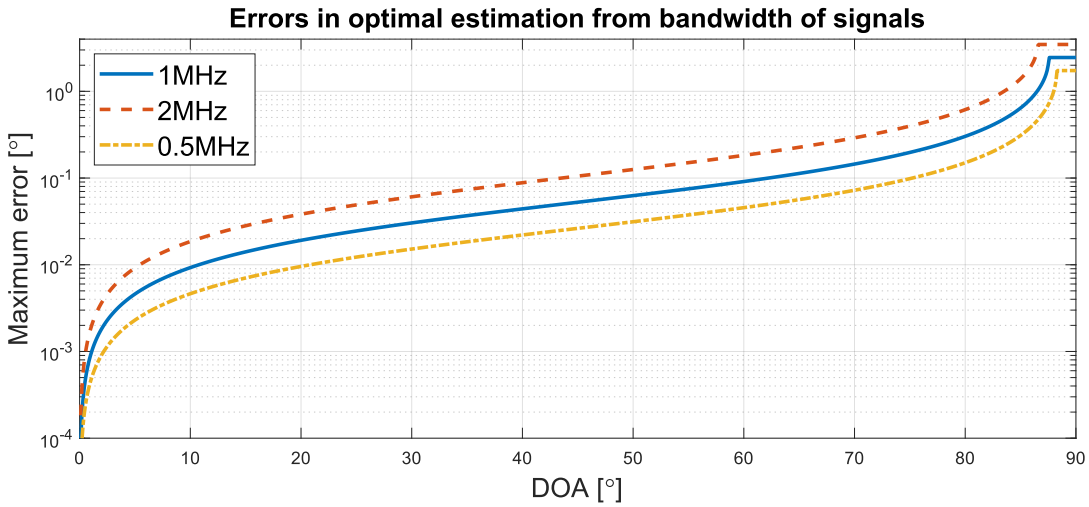

Figure A.1: Theoretical maximum error when optimal DOA estimation is made assuming signal frequency $f = 1090$ MHz. Note that the y-axis is in logarithmic scale.

As seen in Figure A.1, the error is contained at less than a degree within 80°. At around 88°, the errors reach a peak before stagnating. At this point, the introduced error pushes the array phase estimate above the array phase limit corresponding to a 90° DOA.

Generally, the array phase increases for higher DOAs. Hence, any uncertainty in array phase

estimates for larger DOAs, results in greater errors in the azimuth angle estimation. Thus, the errors in estimates naturally grow with larger DOAs, which is seen clearly in the results in Chapter 4.

A.2 Line of sight range

The line of sight range is an important parameter for any radar system. It determines how far away it is possible to detect targets. Because of the curvature of the Earth, how far away the horizon lies is dependent on the altitude above the Earth's surface an observer is placed. In addition, the Earth's atmosphere has different layers, with different properties such as composition, pressure and temperature. This means that, generally, the refractive index of the atmosphere is decreases with altitude. This causes electromagnetic radiation to refract toward the Earth. Therefore, when calculating the line of sight for large altitudes, a factor of $\frac{4}{3}$ is multiplied with the Earth's radius R_e. This means that the line of sight for a platform at height h looking at another platform at the same height becomes

$$R_{los} = 2\sqrt{\left(\frac{4}{3}R_e + h\right)^2 - \left(\frac{4}{3}R_e\right)}. \tag{A.2}$$

Here, the factor of two comes from the fact that R_{los} is measured from the first platform to the horizon and then from the horizon to the second platform.

A.3 Uniform distribution of points on a disk

In circular geometries, uniformly distributing a number of points on a disk can be done two main ways: either by placing points on a surface with a larger area than the disk and then remove the points that misses the disk, or by selecting a random angle, and then selecting a radius for the point from a distribution that makes the final distribution uniform. While the first approach appears to be more straightforward, the latter would mean fewer computations, since no points would have to be randomized again. Given that the final distribution on the disk should be uniform, one can deduct the needed distribution of radii.

To begin with, it is known that the probability distribution over an area is a constant, $p(\vec{r}) = C$, and therefore the integral over the area has to be equal to unity. From this, it is possible to determine the value of C. Given that the disk has a minimum and a maximum radius, $R_{\min}$ and $R_{\max}$, the probability for a point to be located on a disk with area A_{tot} becomes as follows

$$\begin{aligned} \mathbf{P}(r \in A_{tot}) = 1 = \int_{A_{tot}} p(\vec{r})dA = \int_{A_{tot}} CdA = \int_{R_{\min}}^{R_{\max}} C2\pi r dr = C\pi(R_{\max}^2 - R_{\min}^2) \\ C = \frac{1}{\pi(R_{\max}^2 - R_{\min}^2)} \end{aligned} \tag{A.3}$$

meaning that $p(\vec{r}) = C = \frac{1}{\pi(R_{\max}^2 - R_{\min}^2)}$. From this, one notes that $p(r)dr = CdA$ needs to be equal. With $dA = 2\pi r dr$, this yields that $p(r) = 2\pi r C = \frac{2r}{(R_{\max}^2 - R_{\min}^2)}$. The cumulative distribution function is then formed as

$$F(r) = \int_{R_{\min}}^{r} p(r')dr' = \frac{r^2 - R_{\min}^2}{R_{\max}^2 - R_{\min}^2}. \tag{A.4}$$

From the inverse transform method, introducing an uniform random variable $u \in [0, 1]$, one obtains the distribution of radii as

$$r = F^{-1}(u) = \sqrt{R_{\min}^2 + u(R_{\max}^2 - R_{\min}^2)} \tag{A.5}$$

which can be used to generate random samples of radii on a disk from a uniform distribution over the area.

DEPARTMENT OF ELECTRICAL ENGINEERING
CHALMERS UNIVERSITY OF TECHNOLOGY
Gothenburg, Sweden
www.chalmers.se

CHALMERS
UNIVERSITY OF TECHNOLOGY